

RNI: DELENG/2005/15153
Publication: 23rd of every month
Posting: 27th/28th of every month at DPSO

No: DL(E)-01/5079/2023-25
Licensed to post without pre-payment U(E) 28/2023-25
Rs.150

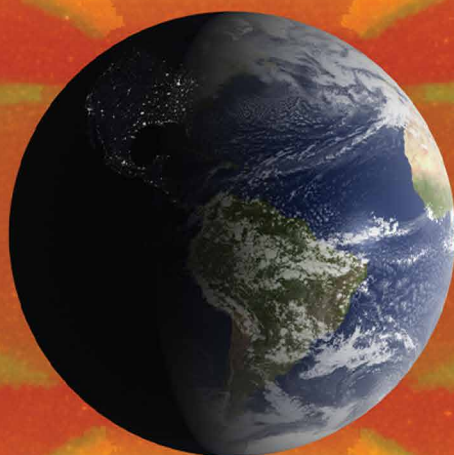
ISSN 0973-2136

www.mycoordinates.org

Coordinates

Volume XIX, Issue 10, October 2023

THE MONTHLY MAGAZINE ON POSITIONING, NAVIGATION AND BEYOND



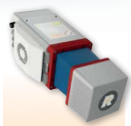
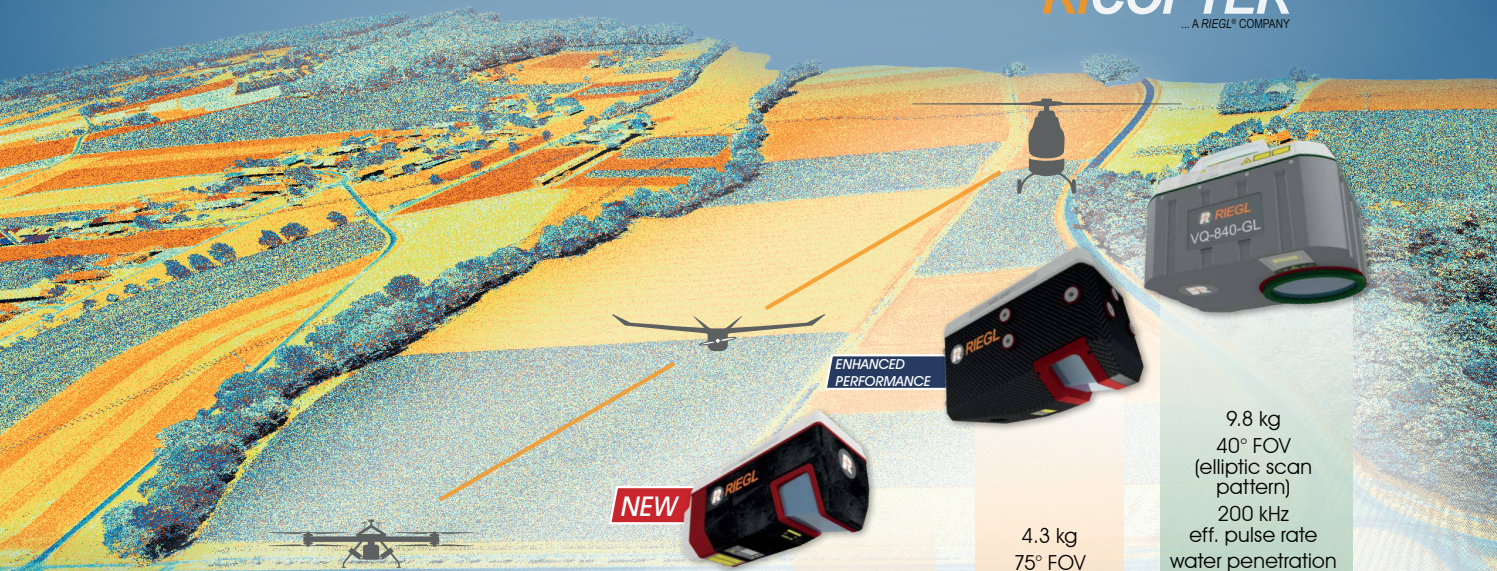
Extreme relativistic electron fluxes in GPS orbit

The investment case for land tenure security in
Sub-Saharan Africa: A cost-benefit analysis

RIEGL UAV LiDAR SENSORS & SYSTEMS

CHOOSE THE SENSOR EXACTLY RIGHT
FOR YOUR SPECIFIC SURVEYING MISSION!

DISTRIBUTED, SUPPORTED AND SERVICED BY
RIICOPTER[®]
... A RIEGL[®] COMPANY



1.6 kg
360° FOV
100 / 200 kHz
eff. pulse rate

extremely lightweight



3.5 kg
360° FOV
1.2 / 1.5 MHz
eff. pulse rate

powerful sensor for various applications in wide area UAV surveying



2.3 kg
100° FOV
2 MHz
eff. pulse rate

NFB (Nadir/ Forward/ Backward) Scanning for an optimal coverage of complex and vertical targets

2.6 kg
100° FOV
2 MHz
eff. pulse rate

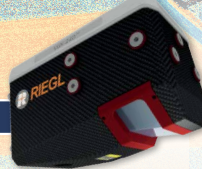
fully integrated IMU/GNSS system

NFB (Nadir/ Forward/ Backward) Scanning for an optimal coverage of complex and vertical targets

2.7 kg
75° FOV
2 MHz
eff. pulse rate

fully integrated IMU/GNSS system

scan speed up to 800 lines/sec, resulting in an optimal line and point distribution; perfectly suited for use on high-speed UAVs



4.3 kg
75° FOV
2 MHz
eff. pulse rate

versatile scanner for use on high-speed UAVs, helicopters or small manned aeroplanes



9.8 kg
40° FOV
(elliptic scan pattern)
200 kHz
eff. pulse rate
water penetration
2 Secchi depths

for topo-bathymetric LiDAR applications

efficient high resolution coastline or shallow water surveying

miniVUX-1UAV
miniVUX-3UAV

for applications using low-flying small or mid-sized multi-rotor UAVs
e.g. mining, topography, forestry, landslide and avalanche monitoring

VUX-1UAV²²
VUX-1LR²²

VUX-120²³

VUX-160²³ / **NEW** VUX-180²⁴

for applications using fixed-wing UAVs
e.g. corridor mapping, city modeling

VUX-240²⁴

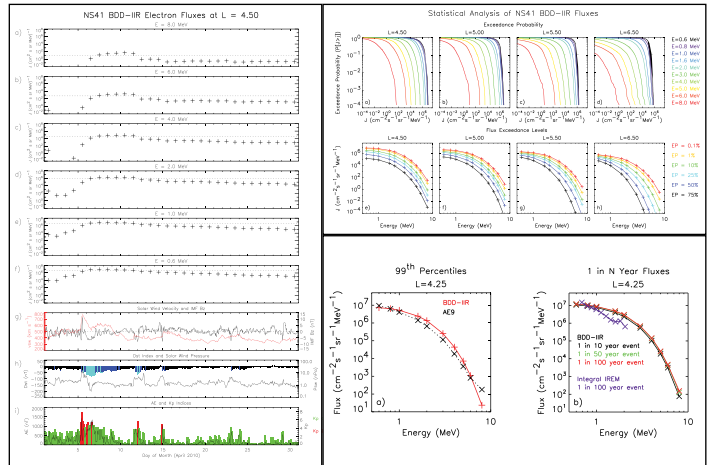
for applications using higher-flying large UAVs or helicopters
e.g. mapping with the need of detailed high-resolution data

VQ-840-GL



Explore the full portfolio of proven
RIEGL LiDAR sensors and systems
www.riegl.com





In this issue

Coordinates Volume 19, Issue 10, October 2023

Articles

- Extreme Relativistic Electron Fluxes in GPS Orbit: Analysis of NS41 BDD-IIR Data** NIGEL P. MEREDITH, THOMAS E. CAYTON, MICHAEL D. CAYTON AND RICHARD B. HORNE 5
- The Investment Case for Land Tenure Security in Sub-Saharan Africa: A Cost-Benefit Analysis** FRANK F K BYAMUGISHA AND NANCY DUBOSSE 19

Cover Image Credit: NASA's Scientific Visualization Studio

Columns

- My Coordinates** EDITORIAL 5 **His Coordinates** ALEXANDER WIECHERT 29 **News** GNSS 31 GIS 32 INDUSTRY 33
- Mark Your Calendar** 34 **Old Coordinates** 35

This issue has been made possible by the support and good wishes of the following individuals and companies

Alexander Wiechert, Frank F K Byamugisha, Michael D. Cayton, Nancy Dubosse, Nigel P. Meredith, Richard B. Horne and Thomas E. Cayton; SBG System, and many others.

Mailing Address

A 002, Mansara Apartments
C 9, Vasundhara Enclave
Delhi 110 096, India.
Phones +91 11 42153861, 98102 33422, 98107 24567

Email

[information] talktous@mycoordinates.org
[editorial] bal@mycoordinates.org
[advertising] sam@mycoordinates.org
[subscriptions] iwant@mycoordinates.org

Web www.mycoordinates.org

Coordinates is an initiative of CMPL that aims to broaden the scope of positioning, navigation and related technologies. CMPL does not necessarily subscribe to the views expressed by the authors in this magazine and may not be held liable for any losses caused directly or indirectly due to the information provided herein. © CMPL, 2023. Reprinting with permission is encouraged; contact the editor for details.

Annual subscription (12 issues)

[India] Rs.1,800* [Overseas] US\$100*

*Excluding postage and handling charges

Printed and published by Sanjay Malaviya on behalf of Coordinates Media Pvt Ltd

Published at A 002 Mansara Apartments, Vasundhara Enclave, Delhi 110096, India.

Printed at Thomson Press (India) Ltd, Mathura Road, Faridabad, India

Editor Bal Krishna

Owner Coordinates Media Pvt Ltd (CMPL)

This issue of Coordinates is of 36 pages, including cover.



Prof M S Swaminathan,

A plant geneticist, agronomist, agricultural scientist,

An advocate of sustainable agriculture,

A proponent of the use of technology in general, and geospatial in particular,

With a caution “not to worship technology, but the outcome one desires”,

And a key architect of India’s ‘green revolution’

Who also warned against ‘greed revolution’

And introduced the vision of ‘evergreen revolution’.

Prof Swaminathan’s contributions have transformed the lives of millions.

And we join millions to remember him.

Bal Krishna, Editor
bal@mycoordinates.org

ADVISORS **Naser El-Sheimy** PEng, CRC Professor, Department of Geomatics Engineering, The University of Calgary Canada, **George Cho** Professor in GIS and the Law, University of Canberra, Australia, **Professor Abbas Rajabifard** Director, Centre for SDI and Land Administration, University of Melbourne, Australia, **Luiz Paulo Souto Fortes** PhD Associate Professor, University of State of Rio Janeiro (UERJ), Brazil, **John Hannah** Professor, School of Surveying, University of Otago, New Zealand

Extreme relativistic electron fluxes in GPS orbit: Analysis of NS41 BDD-IIR data

In this study, an extreme value analysis is conducted of the daily average relativistic electron flux in GPS orbit as a function of position and energy using data from the US NS41 satellite from 10 December 2000 to 25 July 2020

Nigel P. Meredith

British Antarctic Survey, Natural Environment Research Council, Cambridge, United Kingdom

Thomas E. Cayton

Santa Fe, NM, USA

Michael D. Cayton

Santa Fe, NM, USA

Richard B. Horne

British Antarctic Survey, Natural Environment Research Council, Cambridge, United Kingdom

Abstract

Relativistic electrons in the Earth's outer radiation belt are a significant space weather hazard. Satellites in GPS-type orbits pass through the heart of the outer radiation belt where they may be exposed to large fluxes of relativistic electrons. In this study we conduct an extreme value analysis of the daily average relativistic electron flux in Global Positioning System orbit as a function of energy and L using data from the US NS41 satellite from 10 December 2000 to 25 July 2020. The 1 in 10 year flux at $L = 4.5$, in the heart of the outer radiation belt, decreases with increasing energy ranging from $8.2 \times 10^6 \text{ cm}^{-2}\text{s}^{-1}\text{sr}^{-1} \text{ MeV}^{-1}$ at $E = 0.6 \text{ MeV}$ to $33 \text{ cm}^{-2}\text{s}^{-1}\text{sr}^{-1} \text{ MeV}^{-1}$ at $E = 8.0 \text{ MeV}$. The 1 in 100 year is a factor of 1.1–1.7 larger than the corresponding 1 in 10 year event. The 1 in 10 year flux at $L = 6.5$, on field lines which map to the vicinity of geostationary orbit, decrease with increasing energy ranging from $6.2 \times 10^5 \text{ cm}^{-2}\text{s}^{-1}\text{sr}^{-1} \text{ MeV}^{-1}$ at $E = 0.6 \text{ MeV}$ to $0.48 \text{ cm}^{-2}\text{s}^{-1}\text{sr}^{-1} \text{ MeV}^{-1}$ at $E = 8.0 \text{ MeV}$. Here, the 1 in 100 year event is a factor of 1.1–13 times larger than the corresponding 1 in 10 year event, with the value of the factor increasing with increasing energy. Our analysis suggests that the fluxes of relativistic electrons with energies in the range $0.6 \leq E \leq 2.0 \text{ MeV}$ in the region $4.25 \leq L \leq 4.75$ have an upper bound. In contrast, further out and at higher energies the fluxes of relativistic electrons are largely unbounded.

Plain language summary

Relativistic electrons in the Earth's outer radiation belt are a significant space weather hazard. Global Navigation Satellite Systems such as the US Global Positioning System (GPS), the European Galileo navigation system, the Russian GLONASS system, and the Chinese Beidou system operate in medium Earth orbit at altitudes between 19,000 and 24,000 km. They all pass through the heart of the outer radiation belt where they may be exposed to large fluxes of relativistic electrons. In this study we conduct an extreme value analysis of the daily average relativistic electron flux in GPS orbit as a function of position and energy using data from the US NS41 satellite from 10 December 2000 to 25 July 2020. We determine the 1 in 10, 1 in 50 and 1 in 100 year relativistic electron flux levels as a function of position and energy. The 1 in N year relativistic electron fluxes determined here serve as benchmarks against which to compare other extreme space weather events and to help assess the potential impact of an extreme space weather event.

Introduction

Modern society is increasingly reliant on satellites for a wide variety of applications including communication, navigation, Earth observation, and defense. For example, in 2021, the overall global space economy generated revenues of \$386 billion, an increase of 4% compared

to 2020 (Satellite Industry Association, 2022). This ever growing infrastructure is increasingly vulnerable to the potentially damaging effects of space weather (Krausmann, 2011). The concern at government level in the UK is such that severe space weather was added to the UK National Risk Register of Civil Emergencies in 2011, where the likelihood of the reasonable worst case scenario occurring in the next year is currently estimated to be between 1 in 20 and 1 in 100 (HM National Risk Register, 2020).

The impacts of space weather on satellite operations range from momentary interruptions of service to total loss of capabilities when a satellite fails. For example, during a major storm in 2003, 47 satellites experienced anomalies, more than 10 satellites were out of action for more than 1 day, and the joint US-Japanese US\$640M Midori 2 environmental research satellite was a complete loss (Webb & Allen, 2004).

Relativistic electrons ($E > 0.5$ MeV) are a major source of radiation damage to satellites. These, so-called “killer” electrons can penetrate satellite surfaces and embed themselves in insulating materials and ungrounded conductors. Here, the charge can accumulate over time resulting in the build up of high electric fields which may eventually exceed breakdown levels (Frederickson et al., 1991; Rodgers & Ryden, 2001). The subsequent discharge can cause electric circuit upsets, damage components and, in exceptional cases, prove fatal for a satellite (e.g., Koons & Fennel, 2006). Indeed, significant correlations have been found between satellite anomalies and the fluxes of $E > 2$ MeV electrons (Iucci et al., 2005; Wrenn et al., 2002).

Relativistic electrons in near Earth space are generally confined to two distinct regions referred to as the inner and outer radiation belt. The inner radiation belt typically occurs at altitudes from 650 to 6,500 km in the Earth’s magnetic equatorial plane, and the outer radiation belt at altitudes from 13,000 to 40,000 km. The region in between is known

as the slot region and is usually devoid of relativistic electrons. The inner belt is relatively stable with significant variations only occurring during the most intense geomagnetic storms (Baker et al., 2007). In contrast, the outer radiation belt is highly dynamic, especially during geomagnetic storms. Here the fluxes of relativistic electrons may change by orders of magnitude on timescales ranging from minutes to weeks (e.g., Baker et al., 1994; Blake et al., 1992). This variability is controlled by a variety of transport, acceleration and loss mechanisms (e.g., Li & Hudson, 2019; Shprits, Elkington, et al., 2008; Shprits, Subbotin, et al., 2008; Thorne, 2010), all of which become enhanced during enhanced geomagnetic activity. The location of the peak of the flux of relativistic electrons is also highly variable, typically lying at altitudes in the range 14,000–28,000 km (Meredith et al., 2003).

Our critical infrastructure extends to 6.6 Earth radii, encompassing a region which includes the Earth’s inner radiation belt and the bulk of the outer radiation belt. As of 30 April 2022 there were 5,465 operational satellites in Earth orbit, including 4,700 in low Earth orbit (LEO), 140 in Medium Earth Orbit (MEO), 60 in elliptical orbits and 565 in geostationary orbit (GEO) (<https://www.ucsusa.org/resources/satellite-database>). Most are exposed to relativistic electrons at some or all points in their orbits. Satellites in MEO are exposed to relativistic electrons from the outer edge to the heart of the outer radiation belt while satellites in GEO are exposed to relativistic electrons toward the edge of the outer radiation belt. Satellites in LEO are exposed to relativistic electrons in the inner radiation belt and, for those in high inclination LEO orbits, also to relativistic electrons at high magnetic latitudes where they cross field lines which are connected to the outer radiation belt.

Satellite operators and engineers require realistic estimates of the highest fluxes that are likely to be encountered in a particular satellite orbit to assess the impact extreme events on the satellite fleet and to improve resilience of future

satellites by better design of satellite components if required. Satellite insurers also require this information to ensure satellite operators are doing all they can to reduce risk and to help them evaluate realistic disaster scenarios. Previous studies have determined the 1 in 10 and 1 in 100 year event for relativistic electrons in GEO using data from the Energetic Particle Sensors on board the National Oceanic and Atmospheric Administration (NOAA) GOES satellites (Meredith et al., 2015) and High Earth orbit (HEO) using data from the Radiation Environment Monitor (IREM) on board European Space Agency (ESA’s) INTEGRAL spacecraft (Meredith et al., 2017), for energetic electrons in LEO using data from the Medium Energy Proton and Electron Detectors on board the NOAA POES satellites (Meredith et al., 2016a) and for internal charging currents in MEO using data from the SURF instrument on board ESA’s Giove-A satellite (Meredith et al., 2016b). The results from these studies have been used in the development of space weather reasonable worst case scenarios for the UK National Risk Assessment (Hapgood et al., 2021). Furthermore, the 1 in 100 year relativistic electron fluxes from GEO and HEO were included in the US Space Weather Phase 1 Benchmarks report (US Space Weather Phase 1 Benchmarks, 2018).

Global Navigation Satellite Systems (GNSSs) such as the US Global Positioning System (GPS), the European Galileo navigation system, the Russian GLONASS system, and the Chinese Beidou system operate in MEO at altitudes between 19,000 and 24,000 km. They all thus pass through the heart of the outer radiation belt where they may be exposed to large fluxes of relativistic electrons. GNSS-enabled devices are used ubiquitously all over the world for navigation, positioning, tracking, mapping and timing. For example, in 2021 there were 6.5 billion GNSS devices in use and this is expected to rise to 10.3 billion by 2031 (EUSPA EO & GNSS Market Report, 2022). In 2021 the global downstream market revenue from both GNSS-enabled devices and

The impacts of space weather on satellite operations

range from momentary interruptions of service to total loss of capabilities when a satellite fails

services was 199 billion Euros and this is expected to grow to 492 billion Euros by 2031, largely fueled by expected revenues from added value services (EUSPA EO & GNSS Market Report, 2022). It is therefore important to have a comprehensive understanding of the environment encountered by satellites in GNSS-type orbits and, in particular, knowledge of the likely extremes of this environment to be able to better protect space assets operating in this region.

In this study we use approximately 20 years of data from the US GPS NS41 satellite to determine the 1 in 10, 1 in 50, and 1 in 100 year space weather event for relativistic electrons in GPS orbit as a function of energy and L . We first sorted the data by satellite location and calculated the daily average fluxes as a function of energy, L and time. We then computed probability distributions as a function of energy and L . We then conducted extreme value analyses to determine the 1 in 10, 1 in 50, and 1 in 100 year flux as a function of energy and L . The instrumentation and data analysis are described in Section 2 and the probability distributions are presented in Section 3. The extreme value analysis technique is described in Section 4 and the results are presented in Section 5. Finally, the results are discussed and the conclusions presented in Sections 6 and 7 respectively.

Instrumentation and data analysis

Instrumentation

The data used in this study were collected by the Burst Detector Dosimeter IIR (BDD-IIR) on board the US GPS satellite NS41. NS41 was launched on 10 November 2000 and operated in a circular orbit at an altitude of 20,200 km with an

inclination of 55° and a period of 12 hr. It crossed the magnetic equator around $L = 4.2$ and sampled higher L shells at higher magnetic latitudes. For this study we use data from the entire mission, extending from 10 December 2000 to 25 July 2020.

BDD-IIR is a multi purpose silicon detector system. It features 8 individual channels of a “shield/filter/sensor” design that permits the detector to sample roughly half the celestial sphere while at the same time shielding the silicon sensor elements from most of the incident particle flux. Absorbers in front of the sensors determine the energy thresholds for measuring the incident particle fluxes. The aperture dimensions were chosen in an attempt to achieve equal counting rates in all channels. During on-orbit operation none of the BDD-IIR’s channels appeared to saturate. Background counting rates were found to be well behaved. For each week of data mean values of the counting rates of the 8 channels were compiled from accumulations reported from L values larger than 20. Except for weeks with one or more solar energetic particle (SEP) events, the weekly mean values were used for the background counting rates for each of the 2,520 individual records. During SEPs, the background estimation followed the evolution of the SEP and were time dependent.

The deposited energy thresholds were calibrated carefully (Cayton et al., 1998). Electron response functions for the channels were determined by detailed modeling of the instrument by Monte Carlo methods (Tuszewski et al., 2002). The version of the channel response functions used to compute the fluxes studied here were determined from Monte Carlo simulations that exposed the entire BDD-IIR instrument to isotropic fluxes of mono-energetic electrons (Cayton et al., 2010). These

response functions correspond to incident electrons in the energy range 0.1–10 MeV, and involve no scaling factors.

The electron response functions are most sensitive to the highest energy incident electrons. Any electron spectrum covering the energy range from 0.1 to 10 MeV can be folded with the response functions to predict counting rates in all eight channels due to that spectrum. Adding background counting rates to these yields a set of model counting rate that may be compared directly with the measured rates (corrected for the measured 6 ms dead-time). Best-fitting relativistic-Maxwellian spectra were determined by minimizing the sum of squared differences of a set of model counting rates (background plus ones due the spectrum of electrons) and the set of dead-time corrected measured counting rates. Least-squares fitting was attempted only when three or more of the observed (and corrected) rates exceeded the mean background counting rates by more than 3 standard deviations. Each of the best-fitting spectra covers the energy range 0.1–10 MeV. Commonly observed spectral features (i.e., remarkably exponential shapes) of relativistic electrons in the outer radiation belt (Cayton et al., 1989; Pierrard & Lemaire, 1996; Reagan et al., 1981) provided guidance for the selection of the relativistic Maxwellian as the functional form for these model spectra.

For energies greater than 0.5 MeV, electron fluxes computed from this set of response functions compared very well with pitch-angle resolved ones mapped up B-field lines to NS41 from the Synchronous Orbit Particle Analyzer (SOPA, Version 3) aboard S/C LANL-97A during calendar year 2005; below 0.5 MeV the single-component spectra from BDD-IIR consistently underestimated those mapped from geostationary orbit: an additional spectral component is needed to adequately represent the energetic electron population in the energy range 0.1–0.5 MeV. The standard “space-weather data” used here model the electron spectrum as a single

component; we therefore restrict attention to the relativistic electron population with energies greater than 0.5 MeV.

Single relativistic-Maxwellian fits of the BDD-IIR observations at high magnetic latitude contributed to a density and temperature description of energetic electrons in the Earth's magnetotail (Denton & Cayton, 2011). Using instrument specific response functions evaluated for incident electrons in the energy range 0.1–10 MeV, that involve no scaling factors, the procedure described above yielded consistent spectra for NS41 and 11 other GPS spacecraft during the 5-year interval January 2006 through November 2010: NS48 (BDD-IIRM), and NS53–NS62 (Combined X-ray and Dosimeter). Data from BDD-IIR have been extensively used in the DREAM model (Koller et al., 2007; Reeves et al., 2012), to calculate expected solar array degradation (Messenger et al., 2011) and to characterize relativistic electron flux rise times (Varotsou et al., 2008).

Data Analysis

The NS41 BDD-IIR data used in this study were downloaded from the United States Department of Commerce's NOAA website. Each normal file includes 2,520 records of duration 240 s, corresponding to one GPS-week of data. Each weekly file was examined, and excess records (almost always contained only "fill" values) were eliminated. Of the total of 1024 GPS-weeks during the lifetime of the mission, 31 were missing entirely, 3 included data for 1 day and 1 included data for two days. We used the data from the remaining 989 full weekly files in this study.

Each record includes 15 quantities identified as "differential flux" and the 15 energies at which the flux was evaluated. However, when plotted these quantities appear to be simple exponential functions of energy; they also do not agree with differential fluxes evaluated from the best-fitting parameter values reported in the same record, as described in Cayton et al. (2010). When multiplied by $p^2/2m_e$ the recorded values agree with the fluxes

re-evaluated for the fitting parameters; when the re-evaluated differential fluxes, j , are divided by $p^2/2m_e$, the values of $j/p^2/2m_e$ agree with the recorded ones.

Here p is the relativistic momentum and m_e is the electron rest mass and $p^2/2m_e$ is in units of MeV. The software that produced the version 1.09 space-weather files divides the evaluated differential flux by $p^2/2m_e$ before outputting the values. The 15 quantities in each record called "differential flux" are actually phase space densities in the units $\text{cm}^{-2} \text{s}^{-1} \text{MeV}^{-2}$. Bona fide differential fluxes in units $\text{cm}^{-2} \text{s}^{-1} \text{MeV}^{-1}$ may be calculated directly from the phase space

densities reported in the version 1.09 space-weather files by multiplying each value by the appropriate energy factor $E(1 + E/2E_0)$, where E is the electron energy and E_0 is the electron rest mass energy, both in units of MeV. Channel counting rates and evaluated electron phase space densities were plotted; any observed space glitches were eliminated; any out-of-phase coordinates, adjusted; any values containing system-test remnants were replaced by the average of the value before and the value after the affected one. Under normal conditions a system test was executed once each day and affected one of the 360 records for that day.

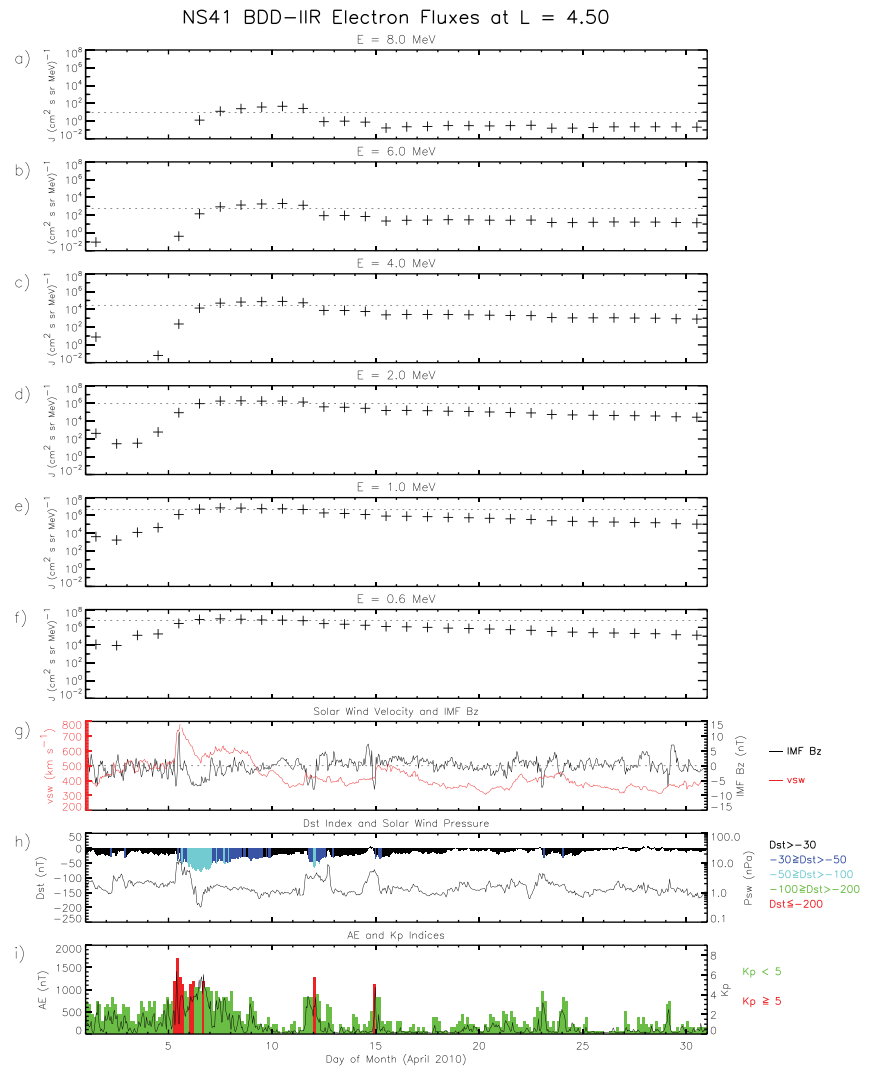


Figure 1. Summary plot of the NS41 Burst Detector Dosimeter IIR electron flux at $L = 4.5$ for April 2010. (a–f) The electron flux at $E = 8.0, 6.0, 4.0, 2.0, 1.0,$ and 0.6 MeV, respectively; (g) the solar wind speed (red trace) and Interplanetary Magnetic Field Bz (black trace); (h) the Dst index (color coded) and solar wind pressure (black trace); and (i) the Kp (color coded) and AE (black trace) indices. The dotted lines in panels a–f represent the 1% exceedance level at each respective energy.

Electron phase space densities at 10 energies (0.6, 0.8, 1.0, 1.6, 2.0, 3.0, 4.0, 5.0, 6.0, and 8.0 MeV) were written into separate files for each crossing of 12

specific L -shell values (4.25, 4.50, 4.75, 5.00, 5.25, 5.50, 5.75, 6.00, 6.25, 6.50, 6.75, and 7.00). Here L is the McIlwain L value calculated using the International Geomagnetic Reference Field internal field and the Olson-Pfizer quiet-time external field (Olson & Pfizer, 1977). NS41 crosses each of the specified L -shells as many as 8 times each day. The phase space densities were then plotted as a function of time for each energy and L value to verify the absence of outliers and other peculiarities in the data. Electron differential fluxes were then calculated from these phase space densities by multiplying each by the corresponding energy factor (0.95225, 1.4262, 1.9785, 4.1049, 5.9139, 11.806, 19.656, 29.462, 41.225, and 70.622). Daily averaged fluxes were then compiled for each of the specified L -shells.

An example monthly summary plot of the daily average electron flux in the heart of the outer radiation belt at $L = 4.5$, is shown in Figure 1 for April 2010. To put the data into context the figure also shows relevant geophysical indices and solar wind parameters. Figure 1 shows (a–f) the electron flux at $E = 8.0, 6.0, 4.0, 2.0, 1.0,$ and 0.6 MeV, respectively; (g) the solar wind speed (red trace) and Interplanetary Magnetic Field (IMF) B_z (black trace); (h) the Dst index (color coded) and solar wind pressure (black trace); and (i) the Kp (color coded) and AE (black trace) indices. The dotted lines in panels a–f represent the 1% exceedance level at each respective energy. The 1% exceedance level is exceeded for a number of days at each energy, with the peak values at each energy being the largest fluxes at that energy observed during the entire mission. These large fluxes are associated with several days of enhanced geomagnetic activity followed by a moderate geomagnetic storm that began on 5 April 2010.

To examine the behavior of the fluxes on a longer timescale we also plotted the electron fluxes for each year as a function of time for each energy and L value. Figure 2 shows one such summary plot of the daily average electron flux

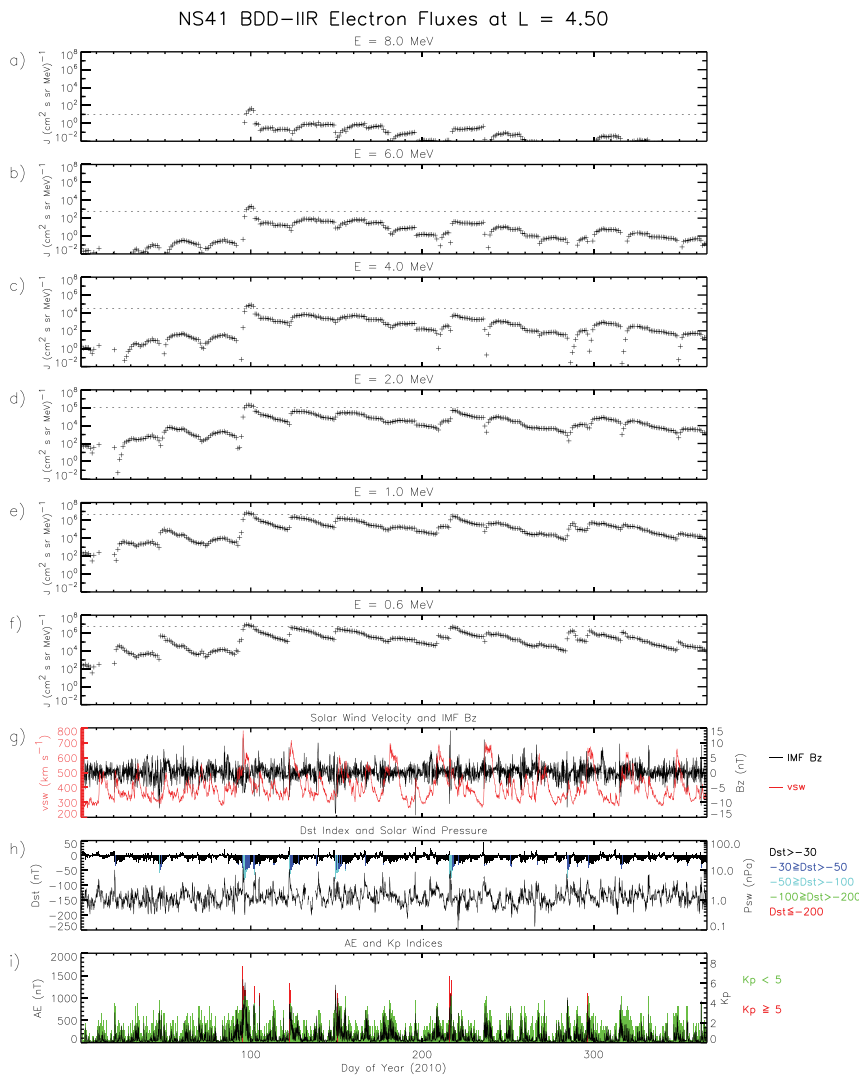


Figure 2. Summary plot of the NS41 Burst Detector Dosimeter IIR electron flux at $L = 4.5$ for 2010. (a–f) The electron flux at $E = 8.0, 6.0, 4.0, 2.0, 1.0,$ and 0.6 MeV, respectively; (g) the solar wind speed (red trace) and Interplanetary Magnetic Field B_z (black trace); (h) the Dst index (color coded) and solar wind pressure (black trace); and (i) the Kp (color coded) and AE (black trace) indices. The dotted lines in panels a–f represent the 1% exceedance level at each respective energy.

Table 1 Largest Electron Fluxes Observed at $E = 1.0, 2.0,$ and 4.0 MeV at $L = 4.5$					
1.0 MeV		2.0 MeV		4.0 MeV	
Flux ($\text{cm}^2\text{ssrMeV}^{-1}$)	Date	Flux ($\text{cm}^2\text{ssrMeV}^{-1}$)	Date	Flux ($\text{cm}^2\text{ssrMeV}^{-1}$)	Date
7.02×10^6	07 April 2010	1.98×10^6	08 April 2010	7.83×10^4	10 April 2010
6.67×10^6	20 January 2005	1.93×10^6	14 September 2005	7.28×10^4	09 April 2010
6.64×10^6	08 April 2010	1.87×10^6	07 April 2010	6.99×10^4	14 September 2005
6.21×10^6	14 September 2005	1.86×10^6	10 April 2010	6.59×10^4	08 April 2010
6.08×10^6	24 July 2004	1.85×10^6	09 April 2010	6.21×10^4	30 July 2004
5.88×10^6	18 May 2005	1.73×10^6	20 January 2005	6.10×10^4	21 September 2003
5.83×10^6	20 September 2003	1.72×10^6	21 September 2003	5.97×10^4	29 July 2004
5.80×10^6	19 January 2005	1.61×10^6	20 September 2003	5.88×10^4	22 September 2003
5.70×10^6	09 April 2010	1.59×10^6	22 September 2003	5.72×10^4	23 September 2003
5.68×10^6	16 April 2006	1.55×10^6	13 September 2005	5.53×10^4	31 July 2004

at $L = 4.5$ for 2010, in a similar format to Figure 1. At each energy the fluxes are characterized by relatively rapid increases followed by gradual decays lasting many days. The figure shows that in 2010 the 1% exceedance level was only exceeded during the April geomagnetic storm, although several other flux increases approached the 1% levels.

Statistics

The top 10 daily average fluxes of $E = 1.0$, $E = 2.0$, and $E = 4.0$ MeV electrons at $L = 4.5$, representative of the heart of the outer radiation belt, and $L = 6.5$ at higher magnetic latitudes on field lines that map to geostationary orbit, are tabulated in Tables 1 and 2 respectively. The largest

daily average $E = 1.0$, $E = 2.0$, and $E = 4.0$ MeV electron fluxes observed at $L = 4.5$ were 7.02×10^6 , 1.98×10^6 , and 7.83×10^4 $\text{cm}^{-2} \text{s}^{-1} \text{sr}^{-1} \text{MeV}^{-1}$ respectively, occurring on 7, 8 and 10 April 2010 respectively. Further out, at $L = 6.5$, the largest fluxes of $E = 1.0$, $E = 2.0$, and $E = 4.0$ MeV electrons were factors of 14, 14, and 18 lower for each energy respectively and all occurred on 10 April 2010. We note that the flux near the magnetic equator at $L = 6.5$ could be higher if the equatorial pitch angle distribution is peaked near 90° as electrons mirroring near the equator are not sampled at higher magnetic latitudes.

The distributions of the daily average electron fluxes at $L = 4.5, 5.0, 5.5,$ and 6.5 are shown in Figures 3a–3d respectively. The observed flux for any given exceedance probability decreases with increasing energy at each value of L , as expected for relativistic electrons in the outer radiation belt where fluxes decrease with increasing energy. At any given energy and exceedance probability the observed flux also decreases with increasing L . There is also a tendency for the gradient of the exceedance probability for the top 1% of the fluxes to steepen with decreasing energy as can be seen from $E = 8.0$ through to $E = 0.6$ MeV, red to black traces, at $L = 6.5$ (Figure 3d). In other words, for exceedance probabilities less than 1%, there is only a small fractional increase in the flux at low energies compared to that at higher energies. The steepening also gets larger going to lower L . In the heart of the outer radiation belt, at $L = 4.5$, the largest observed fluxes cover over five orders of magnitude, ranging from $8.90 \times 10^6 \text{ cm}^{-2} \text{ s}^{-1} \text{ sr}^{-1} \text{ MeV}^{-1}$ at $E = 0.6$ MeV to $46 \text{ cm}^{-2} \text{ s}^{-1} \text{ sr}^{-1} \text{ MeV}^{-1}$ at $E = 8.0$ MeV. Further out, at $L = 6.5$, the largest fluxes are factors of 14 and 34 lower at $E = 0.6$ and 8.0 MeV respectively.

The fluxes corresponding to selected exceedance probabilities at $L = 4.5, 5.0, 5.5,$ and 6.5 are shown in Figures 3e–3h respectively. The flux for a given exceedance probability decreases with increasing energy. At $L = 4.5$ the 1% exceedance level ranges from $5.67 \times 10^6 \text{ cm}^{-2} \text{ s}^{-1} \text{ sr}^{-1} \text{ MeV}^{-1}$ at $E = 0.6$ MeV to

1.0 MeV		2.0 MeV		4.0 MeV	
Flux ($\text{cm}^2 \text{srMeV}^{-1}$) ⁻¹	Date	Flux ($\text{cm}^2 \text{srMeV}^{-1}$) ⁻¹	Date	Flux ($\text{cm}^2 \text{srMeV}^{-1}$) ⁻¹	Date
5.20×10^5	10 April 2010	1.45×10^5	10 April 2010	4.32×10^3	10 April 2010
4.97×10^5	30 July 2004	1.21×10^5	30 July 2004	2.74×10^3	30 July 2004
3.89×10^5	11 April 2010	8.40×10^4	11 April 2010	1.50×10^3	11 April 2010
3.63×10^5	03 April 2008	7.20×10^4	03 April 2008	1.45×10^3	21 September 2005
3.29×10^5	12 May 2016	6.96×10^4	31 July 2004	1.41×10^3	31 July 2004
3.26×10^5	30 August 2018	6.73×10^4	05 August 2003	1.35×10^3	05 August 2003
3.24×10^5	09 April 2005	6.48×10^4	18 October 2017	1.33×10^3	15 November 2004
3.21×10^5	31 July 2004	6.43×10^4	12 May 2016	1.32×10^3	04 August 2004
3.18×10^5	18 October 2017	6.27×10^4	02 April 2008	1.19×10^3	18 December 2003
3.07×10^5	02 April 2008	6.02×10^4	30 August 2018	1.17×10^3	19 April 2006

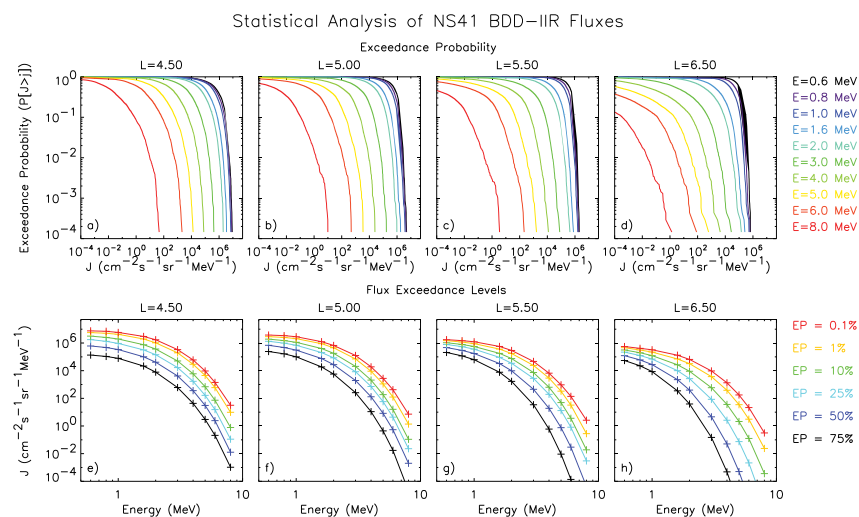


Figure 3. Plots of the exceedance probabilities for (a) $L = 4.5$, (b) $L = 5.0$, (c) $L = 5.5$, and (d) $L = 6.5$ for each electron energy and flux exceedance levels as a function of energy at (e) $L = 4.5$, (f) $L = 5.0$, (g) $L = 5.5$, and (h) $L = 6.5$.

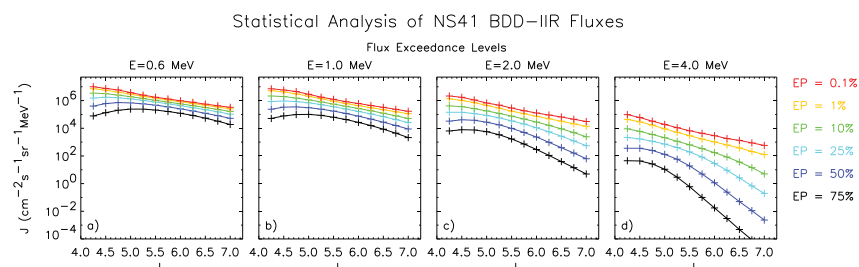


Figure 4. Plots of the flux exceedance levels as a function of L for (a) $E = 0.6$, (b) $E = 1.0$, (c) $E = 2.0$, and (d) $E = 4.0$ MeV electrons.

$9.78 \text{ cm}^{-2} \text{ s}^{-1} \text{ sr}^{-1} \text{ MeV}^{-1}$ at $E = 8.0 \text{ MeV}$. Further out, at $L = 6.5$, the 1% exceedance levels are factors of 12 and 409 lower at $E = 0.6$ and 8.0 MeV respectively.

The fluxes for selected exceedance levels are shown as a function of L for four selected energies in Figure 4. The median flux of relativistic electrons in the energy range $0.6 \leq E \leq 2.0 \text{ MeV}$ peaks at $L = 4.75$. However, for exceedance levels below 10%, for any given energy, the fluxes peak at $L = 4.25$, the inner limit of the observations, and decrease with increasing L .

Extreme value analysis

The main objective of this study is to determine the 1 in 10 and 1 in 100 year daily average electron flux for the specified energies and L shells. Since daily averages are available and to compare with our previous studies (Meredith et al., 2015, 2016a, 2016b, 2017), we use the exceedances over a high threshold approach (Dey & Das, 2016; Thomson et al., 2011). For this approach, also known as the Peaks Over Threshold method, the appropriate distribution function is the generalized Pareto distribution (GPD), first introduced by Picklands (1975). This model assumes that the underlying physics is similar during extreme events. For example, it assumes that an extremely rare event doesn't occur with a completely different set of characteristics, not seen before. This assumption is likely to be valid for the outer radiation belt studied here, but would not necessarily hold for the inner radiation belt (e.g., Shprits et al., 2011). This approach has been used successfully in many fields to estimate, for example, extremes of rainfall (e.g., Li et al., 2005), surface temperature (e.g., Nogaj et al., 2006), geomagnetic storm events (Tsubouchi & Omura, 2007), wind speed (e.g., Della-Marta et al., 2009), geomagnetic activity (Thomson et al., 2011), storm surge (e.g., Tebaldi et al., 2012), hurricane damage (Dey & Das, 2016), and the probability of Carrington-like solar flares (Elvidge & Angling, 2018).

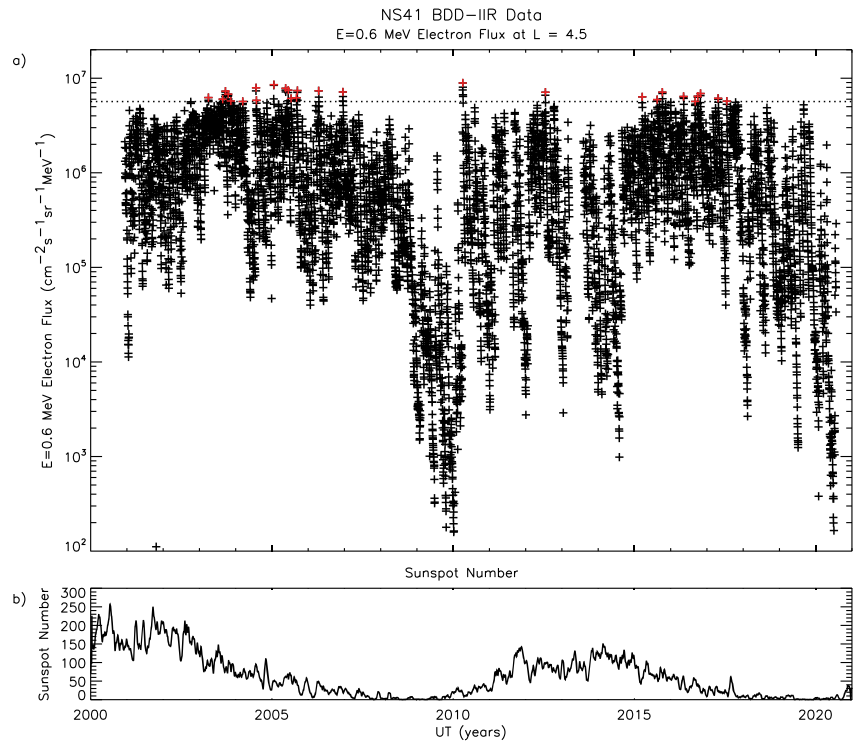


Figure 5. Plot of the $E = 0.6 \text{ MeV}$ daily average electron flux as a function of time at $L = 4.5$. (a) The 1% exceedance level, chosen as the threshold for the extreme value analysis, is shown as a dotted line and the cluster maxima are coded red. (b) Trace of the sunspot number as a function of time.

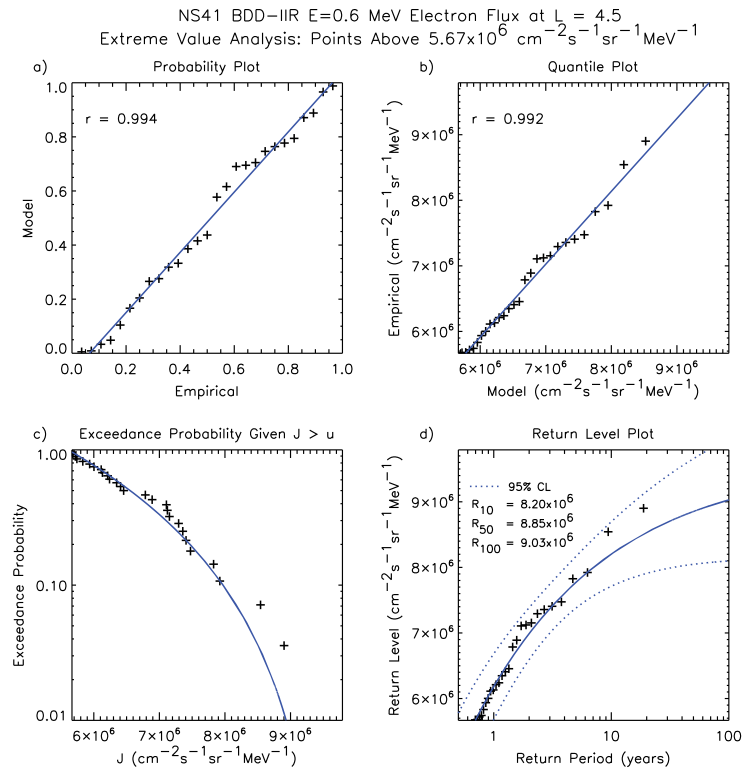


Figure 6. Extreme value analysis for the $E = 0.6 \text{ MeV}$ daily average electron flux at $L = 4.5$. (a) Probability plot, (b) quantile plot, (c) the exceedance probability given $J > u$, and (d) the return level plot.

The threshold at each energy and L should be low enough to include a meaningful number of data points and high enough to capture the behavior of the tail of the distribution. Based on experience analyzing other satellite data sets (e.g., Meredith et al., 2015, 2017), for each energy and L we set the threshold at the 1% exceedance level. We declustered the data by assuming a cluster to be active until three consecutive daily average values fell below the chosen threshold. We then fit the GPD (Coles, 2001; Picklands, 1975) to the cluster maxima for each specified energy and L shell using the `ismev` library routine `gpd.fit` provided in the R statistical package (R Foundation for Statistical Computing, 2008). The GPD may be written as:

$$G(y) = 1 - \left(1 + \frac{\xi y}{\sigma}\right)^{-\frac{1}{\xi}} \quad (1)$$

where $y = (x - u)$ are the exceedances, x are the cluster maxima above the chosen threshold, u , ξ is the shape parameter and σ the scale parameter (Coles, 2001). The sign of the shape parameter provides important information on the behavior of tail of the distribution. If ξ is positive the distribution has no upper limit whereas if ξ is negative the distribution has an upper bound. The level, x_{N_p} , which is exceeded on average once every N years may be expressed in terms of ξ and σ as:

$$x_N = u + \frac{\sigma}{\xi} \left((N n_d n_c / n_{tot})^\xi - 1 \right) \quad (2)$$

where n_c is the number of clusters, n_{tot} is the total number of data points and $n_d = 365.25$ is the average number of days in any given year (Coles, 2001).

Results

To demonstrate the method used we first show the results for $E = 0.6$ MeV electrons at $L = 4.5$. The $E = 0.6$ MeV daily average electron flux is shown as a function of time in Figure 5a. The 1% exceedance level of $5.67 \times 10^6 \text{ cm}^{-2} \text{ s}^{-1} \text{ sr}^{-1} \text{ MeV}^{-1}$, chosen as the threshold for the extreme value analysis, is shown as the dotted line and the cluster maxima are coded red. A trace of the 27-day average sunspot number is shown in Figure 5b. The largest fluxes of $E = 0.6$ MeV electrons at $L = 4.5$ are largely seen from 2003–2008 and 2015–2018 during the declining phases of solar cycles 23 and 24 respectively, with lower fluxes typically being seen around the solar minima and solar maxima.

The scale and shape parameters for the fit to the cluster maxima of $E = 0.6$ MeV electrons at $L = 4.5$ are determined to be $(1.5 \pm 0.01) \times 10^6$ and -0.39 ± 0.08 respectively. The shape parameter is

negative, suggesting that the flux of 0.6 MeV electrons at $L = 4.5$ tends to a limiting value. To assess the quality of the fitted GPD model we compare the empirical and modeled probabilities and quantiles (Coles, 2001). Figure 6a shows the probability plot for the cluster maxima of the $E = 0.6$ MeV electron flux. Here we plot the modeled probability, $G(y)$ against the empirical probability, that X exceeds some value x given that it already exceeds a threshold u . The best fit straight line to the data points is shown in blue and has a correlation coefficient of 0.994. Figure 6b shows the quantile plot for the cluster maxima of the $E = 0.6$ MeV electron flux. Here we plot the modeled fluxes against the empirical fluxes. The best fit straight line is again shown in blue and has a correlation coefficient of 0.992. The fact that both fits are approximately linear suggests that the generalized Pareto model is a good method for modeling the exceedances (e.g., Coles, 2001).

Figure 6c shows the exceedance probability of the cluster maxima above the threshold value of $5.67 \times 10^6 \text{ cm}^{-2} \text{ s}^{-1} \text{ sr}^{-1} \text{ MeV}^{-1}$, $(P[J > j | J > u])$ (black symbols), together with the maximum likelihood fit (blue line). Figure 6d shows the flux that is exceeded on average once every N years as a function of N for the declustered $E = 0.6$ MeV electron flux. The 1 in N year return level determined from Equation 2 is shown as the solid blue line and the symbols represent the experimental return levels. The 95% confidence interval of the 1 in N year return levels are shown as the dotted blue lines. The 1 in 10, 1 in 50, and 1 in 100 year $E = 0.6$ MeV electron fluxes at $L = 4.5$ are $(8.20 \pm 0.49) \times 10^6$, $(8.85 \pm 0.81) \times 10^6$, and $(9.03 \pm 0.93) \times 10^6 \text{ cm}^{-2} \text{ s}^{-1} \text{ sr}^{-1} \text{ MeV}^{-1}$, where the quoted errors represent the 95% confidence limits.

We repeated the analysis for each electron energy at each value of L and determined the corresponding 1 in N year fluxes. The return levels are shown as a function of energy at $L = 4.5, 5.0, 5.5$, and 6.5 in Figures 7a–7d respectively. The 1 in N year fluxes decrease with increasing energy and L . At $L = 4.5$ there is very little

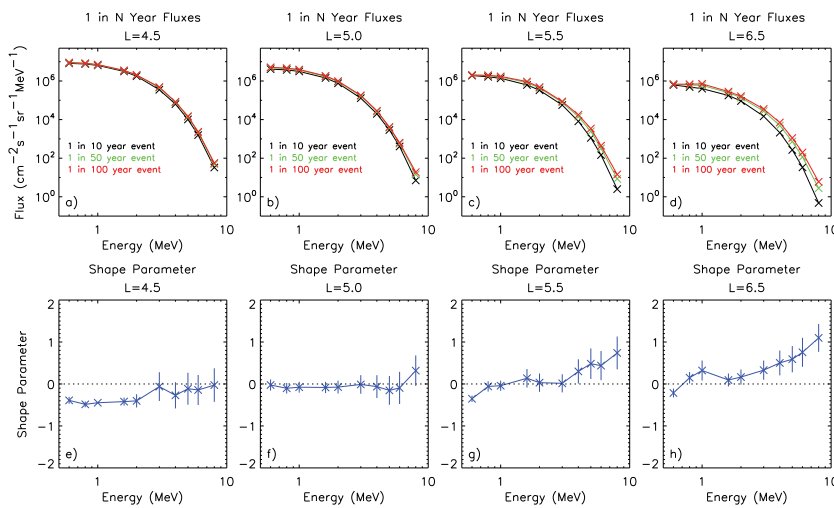


Figure 7. Plots of the 1 in N year electron flux as a function of energy for $N = 10$ (black trace and symbols), 50 (green trace and symbols), and 100 years (red trace and symbols) for (a) $L = 4.5$, (b) $L = 5.0$, (c) $L = 5.5$, and (d) $L = 6.5$ and the shape parameter as a function of energy for (e) $L = 4.5$, (f) $L = 5.0$, (g) $L = 5.5$, and (h) $L = 6.5$.

difference between the 1 in 10 and 1 in 100 year events (Figure 7a). However, further out, there is an increasing tendency for more variation in the 1 in 10 and 1 in 100 year events, particularly at higher energies, with the threshold at which the variability increases decreasing with increasing L (Figures 7b–7d). Specifically, at $L = 4.5$ (Figure 7a), the 1 in 10 year flux (black line) ranges from $8.2 \times 10^6 \text{ cm}^{-2} \text{ s}^{-1} \text{ sr}^{-1} \text{ MeV}^{-1}$ at $E = 0.6 \text{ MeV}$ to $33 \text{ cm}^{-2} \text{ s}^{-1} \text{ sr}^{-1} \text{ MeV}^{-1}$ at $E = 8.0 \text{ MeV}$, with the 1 in 100 year event (red line) being a factor of 1.1–1.7 larger than the corresponding 1 in 10 year event. Further out, at $L = 6.5$ (Figure 7c), the 1 in 10 year flux (black line) ranges from $6.2 \times 10^5 \text{ cm}^{-2} \text{ s}^{-1} \text{ sr}^{-1} \text{ MeV}^{-1}$ at $E = 0.6 \text{ MeV}$ to $0.48 \text{ cm}^{-2} \text{ s}^{-1} \text{ sr}^{-1} \text{ MeV}^{-1}$ at $E = 8.0 \text{ MeV}$, with the 1 in 100 event being a factor of 1.1–13 times larger than the corresponding 1 in 10 year event.

The shape parameter from the extreme value analysis is shown as a function of energy at $L = 4.5, 5.0, 5.5,$ and 6.5 in Figures 7e–7h respectively. In the heart of the outer radiation belt, at $L = 4.5$ (Figure 7e), the shape parameter is robustly negative, with the maximum of the 95% confidence interval lying below 0, at energies in the range $0.6 \leq E \leq 2.0 \text{ MeV}$, suggesting that the electron fluxes in this region and at these energies are bounded and tend to a limiting value. At higher energies the shape parameter remains largely negative in this region although the error bars include positive values, making it difficult to be conclusive about the whether the fluxes are bounded or unbounded at $E \geq 3 \text{ MeV}$. Similar behavior is observed at $L = 4.25$ and 4.75 (not shown). Moving out in L , at $L = 5.0$ (Figure 7f) and $L = 5.25$ (not shown), the shape parameter is mostly negative, but with error bars that includes both positive and negative values, again making it difficult to be conclusive about whether the fluxes are bounded or unbounded in this region. Further out there is an increasing tendency for the shape parameter to become robustly positive at higher energies from $E \geq 4.0 \text{ MeV}$ at $L = 5.5$ (Figure 7g), from $E \geq 3 \text{ MeV}$ at $L = 6.5$ (Figure 7h) and from $E \geq 1 \text{ MeV}$ at $L = 7.0$ (not shown). This suggests that the

relativistic electron fluxes in these regions and at these energies have no upper bound. Interestingly, the shape parameter is robustly negative for the $E = 0.6 \text{ MeV}$ electrons in this region (Figures 7g and 7h), suggesting that the 0.6 MeV electron fluxes also have an upper bound at larger L all the way out to $L = 7.0$ (not shown).

The 1 in 10, 1 in 50, and 1 in 100 year fluxes are summarized as a function of L for each energy in Figures 8a–8c respectively. The 1 in 100 year flux of $E = 0.6 \text{ MeV}$ electrons decreases with increasing L ranging from to $1.2 \times 10^7 \text{ cm}^{-2} \text{ s}^{-1} \text{ sr}^{-1} \text{ MeV}^{-1}$ at $L = 4.25$ to $3.8 \times 10^5 \text{ cm}^{-2} \text{ s}^{-1} \text{ sr}^{-1} \text{ MeV}^{-1}$ at $L = 7.00$, and are factors of 1.1 times the corresponding 1 in 10 year flux. At higher energies, the 1 in 100 year flux of $E = 2.0 \text{ MeV}$ electrons ranges from to $3.0 \times 10^6 \text{ cm}^{-2} \text{ s}^{-1} \text{ sr}^{-1} \text{ MeV}^{-1}$ at $L = 4.25$ to $1.1 \times 10^5 \text{ cm}^{-2} \text{ s}^{-1} \text{ sr}^{-1} \text{ MeV}^{-1}$ at $L = 7.00$ and are factors of 1.3 and 2.2 larger than the corresponding 1 in 10 year fluxes respectively.

Discussion

Some of the largest daily average fluxes encountered during the entire mission were observed during the 6 April 2010

geomagnetic storm (Figure 1). This was a relatively moderate geomagnetic storm with a minimum Dst of -81 nT at 14:00 UT on 6 April 2010. The recovery phase of this storm lasted for approximately 5 days, the first 4 days of which were associated with enhanced geomagnetic activity. Interestingly, the relativistic electron fluxes at $L = 4.5$ had started to rise from 2 April, prior to the arrival of the geomagnetic storm due to a period of IMF Bz fluctuating about zero and enhanced geomagnetic activity as monitored by the AE index. The largest daily averaged fluxes of relativistic electrons in the heart of the outer radiation belt at $L = 4.5$ at each energy were observed during this storm. Here the flux peaks ranged from $8.9 \times 10^6 \text{ cm}^{-2} \text{ s}^{-1} \text{ sr}^{-1} \text{ MeV}^{-1}$ at $E = 0.6 \text{ MeV}$ to $46 \text{ cm}^{-2} \text{ s}^{-1} \text{ sr}^{-1} \text{ MeV}^{-1}$ at $E = 8.0 \text{ MeV}$ on the 7 and 10 April respectively. The large flux levels were also sustained, remaining above the 1% exceedance level for 5 days. Further out, at $L = 6.5$, the largest daily average fluxes were observed at all energies in the range $0.8 \leq E \leq 8.0 \text{ MeV}$, ranging from $6.0 \times 10^5 \text{ cm}^{-2} \text{ s}^{-1} \text{ sr}^{-1} \text{ MeV}^{-1}$ at $E = 0.8 \text{ MeV}$ to $1.36 \text{ cm}^{-2} \text{ s}^{-1} \text{ sr}^{-1} \text{ MeV}^{-1}$ at $E = 8.0 \text{ MeV}$. Here, the high flux level were sustained for a shorter period of time, remaining above the 1% level for 2 days.

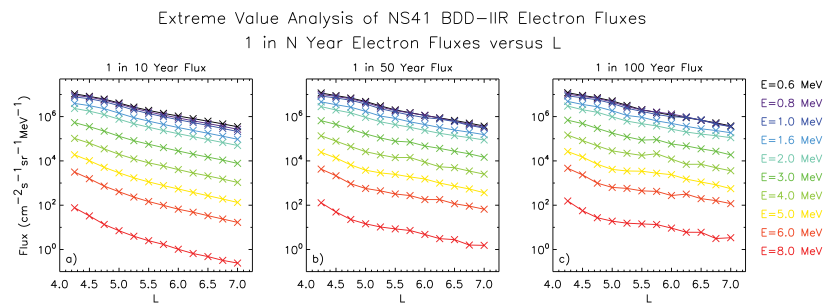


Figure 8. Plots of the 1 in N year electron flux as a function of L for each energy (color-coded) for (a) $N = 10$ years, (b) $N = 50$ years, and (c) $N = 100$ years.

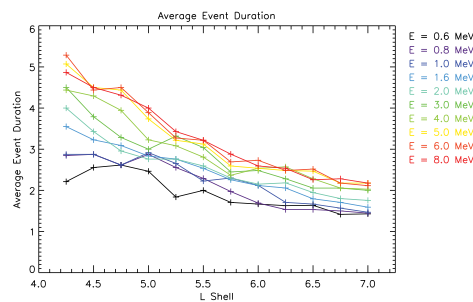


Figure 9. Plots of the average event duration as a function of L for each energy (color-coded).

The largest internal charging currents observed by the top, middle and bottom plates of the SURF instrument on Giove-A between December 2005 and January 2016 also occurred during this event, both at $L^* = 4.75$ near the heart of the outer radiation belt and at $L^* = 6.0$ on field lines that map out close to geostationary orbit (Meredith et al., 2016b). This suggests that the largest observed internal charging currents recorded by each of the SURF plates in these two locations are rarer than would be expected based on the original statistics, with, for example, the empirical return period being of the order of 20 years as opposed to 8.5 years estimated in the original study.

In this study we have focused on the 1 in 10 and 1 in 100 year daily average relativistic electron fluxes as a function of energy and L . However, the duration of the enhanced fluxes associated with the largest events are also important, since charge deposited on insulators and ungrounded conductors builds up over time. Figure 9 shows the average time the flux exceeds the 1% exceedance level for each of the cluster maxima for each energy (color-coded) as a function of L . At $L = 4.5$ the average event duration increases with increasing energy from 2.5 days at 0.6 MeV to 4.4 days at the highest energies. The same trend is seen at larger L , for example, $L = 6.5$, but the average duration is smaller ranging from 1.4 days at $E = 0.6$ MeV to 2.5 days at $E = 8.0$ MeV. Although we are not fitting decay timescales the data indicate that, over the range of energies and L sampled, the timescale for loss is generally smaller at lower energies and higher L .

The conclusion that the fluxes tend to a limiting value in the region $4.25 \leq L \leq 4.75$ at energies in the range $0.6 \leq E \leq 2.0$ MeV is consistent with the findings from a similar analysis of the INTEGRAL IREM data (Meredith et al., 2017). However, the latter study also concluded that the relativistic electrons in this energy range tended to limiting values out to $L^* = 6.0$. Unfortunately, our study does not throw any definitive light on the behavior of the relativistic electron fluxes in the

energy range $0.6 \leq E \leq 2.0$ MeV beyond $L \geq 5.0$ due to the fact that the shape parameter is mostly close to zero with error bars encompassing both positive and negative values. However, at higher

energies and high L the shape parameter is robustly positive, suggesting the fluxes are unbounded at high energy and high L .

It is hard to understand why the fluxes

Table 3
1 in 10 Year, 1 in 100 Year and Limiting Fluxes at $L = 4.5$ and $L = 6.5$

Energy (MeV)	$L = 4.5$			$L = 6.5$		
	1 in 10 yr Flux ($\text{cm}^2\text{ssrMeV}^{-1}$)	1 in 100 yr Flux ($\text{cm}^2\text{ssrMeV}^{-1}$)	Limiting Flux ($\text{cm}^2\text{ssrMeV}^{-1}$)	1 in 10 yr Flux ($\text{cm}^2\text{ssrMeV}^{-1}$)	1 in 100 yr Flux ($\text{cm}^2\text{ssrMeV}^{-1}$)	Limiting Flux ($\text{cm}^2\text{ssrMeV}^{-1}$)
0.6	8.2×10^6	9.0×10^6	9.6×10^6	6.2×10^5	6.9×10^5	7.9×10^5
0.8	7.6×10^6	8.3×10^6	8.6×10^6	4.9×10^5	6.8×10^5	–
1.0	6.4×10^6	7.1×10^6	7.4×10^6	4.0×10^5	7.1×10^5	–
1.6	3.1×10^6	3.5×10^6	3.8×10^6	1.8×10^5	2.8×10^5	–
2.0	1.8×10^6	2.0×10^6	2.2×10^6	9.2×10^4	1.6×10^5	–
3.0	3.5×10^5	4.8×10^5	–	1.5×10^4	3.5×10^4	–
4.0	6.3×10^4	8.3×10^4	–	2.1×10^3	7.0×10^3	–
5.0	1.0×10^4	1.5×10^4	–	2.7×10^2	1.1×10^3	–
6.0	1.6×10^3	2.3×10^3	–	3.4×10^1	2.0×10^2	–
8.0	3.3×10^1	5.6×10^1	–	4.8×10^{-1}	6.0×10^0	–

Table 4
Number of Times the Daily Average Flux Is Within a Factor of Two of the Corresponding 1 in 100 Year Flux

L	$E = 0.6$ MeV	$E = 0.8$ MeV	$E = 1.0$ MeV	$E = 2.0$ MeV	$E = 4.0$ MeV	$E = 6.0$ MeV	$E = 8.0$ MeV
4.25	147	148	134	25	<i>13</i>	<i>6</i>	<i>3</i>
4.50	195	144	126	67	<i>24</i>	<i>12</i>	<i>4</i>
4.75	148	116	99	<i>49</i>	<i>25</i>	<i>14</i>	<i>0</i>
5.00	<i>159</i>	<i>103</i>	<i>98</i>	<i>52</i>	<i>27</i>	<i>8</i>	<i>0</i>
5.25	<i>447</i>	<i>207</i>	<i>124</i>	<i>55</i>	<i>20</i>	<i>8</i>	<i>0</i>
5.50	743	<i>205</i>	<i>114</i>	<i>13</i>	<i>5</i>	<i>2</i>	<i>0</i>
5.75	742	<i>114</i>	<i>47</i>	<i>8</i>	<i>2</i>	<i>0</i>	<i>0</i>
6.00	677	<i>100</i>	<i>19</i>	<i>4</i>	<i>2</i>	<i>0</i>	<i>0</i>
6.25	570	<i>91</i>	<i>22</i>	<i>3</i>	<i>1</i>	<i>0</i>	<i>0</i>
6.50	339	<i>57</i>	<i>12</i>	<i>2</i>	<i>1</i>	<i>0</i>	<i>0</i>
6.75	372	<i>63</i>	<i>15</i>	<i>3</i>	<i>1</i>	<i>0</i>	<i>0</i>
7.00	406	<i>57</i>	<i>13</i>	<i>3</i>	<i>0</i>	<i>0</i>	<i>0</i>

Note. Bounded cases in bold font, unbounded cases in normal font and undetermined cases in italic font.

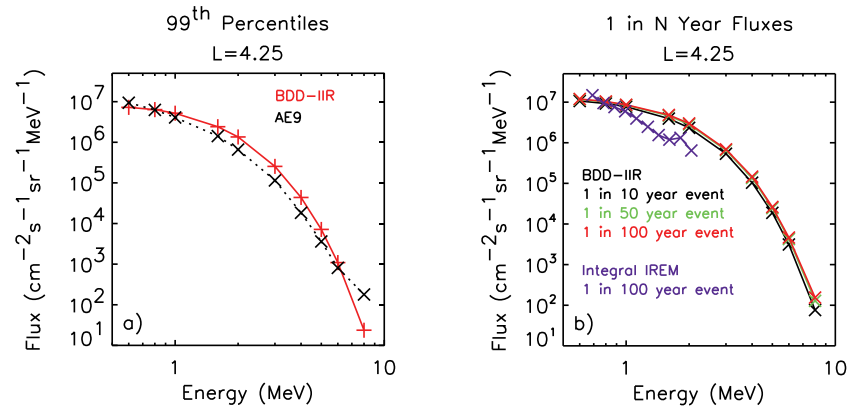


Figure 10. (a) Plot of the 99th percentile of the Burst Detector Dosimeter IIR fluxes at $L = 4.25$ (red trace and symbols) and the 99th percentile of the IRENE AE9 fluxes for a 20,200 km equatorial orbit (black trace and symbols) as a function of energy. (b) Plot of the 1 in N year electron flux at $L = 4.25$ as a function of energy for $N = 10$ (black trace and symbols), 50 (green trace and symbols), and 100 years (red trace and symbols), together with the 1 in 100 year electron flux determined from INTEGRAL IREM (purple trace and symbols).

at the higher energies and high L , for example, $E > 3$ MeV at $L = 6.5$, have no upper bound when the plots of the 1 in N year fluxes are so smooth and the 1 in N year flux levels at the higher energies are orders of magnitude lower than the corresponding flux levels at 0.6 MeV, which are bounded. One possibility is that fluxes approaching the limiting value are extremely rare at higher energy and L , highlighting the inherent difficulty in using 20 years of data to infer the presence or absence of an upper limit which may typically not be reached for 100 years or more. Another possible reason for the difference is that the instrument samples higher L shells at higher magnetic latitudes and there could be some variation in anisotropy that is not captured at higher energy and L .

When the shape parameter is negative, the limiting value, x_L , can be calculated for any given energy and L and is given by

$$x_L = u - \frac{\sigma}{\xi} \quad (3)$$

The limiting fluxes as a function of energy at $L = 4.5$ and $L = 6.5$ are tabulated in Table 3, together with the 1 in 10 and 1 in 100 year fluxes. Here we only tabulate the limiting fluxes when the upper limit of 95% confidence interval of the shape parameter is negative. At $L = 4.5$ the limiting fluxes lie in the range $9.6 \times 10^6 \text{ cm}^{-2} \text{ s}^{-1} \text{ sr}^{-1} \text{ MeV}^{-1}$ at $E = 0.6$ MeV to $2.2 \times 10^6 \text{ cm}^{-2} \text{ s}^{-1} \text{ sr}^{-1} \text{ MeV}^{-1}$ at $E = 2.0$ MeV and are up to factors of 1.26 and 1.07 times larger than the corresponding 1 in 10 and 1 in 100 year fluxes. Further out, at $L = 6.5$ the limiting flux of $E = 0.6$ MeV electrons is $7.9 \times 10^5 \text{ cm}^{-2} \text{ s}^{-1} \text{ sr}^{-1} \text{ MeV}^{-1}$ and is a factor of 1.27 and 1.14 times larger than the corresponding 1 in 10 and 1 in 100 year fluxes.

It is interesting to note that when the fluxes tend to limiting values the 1 in 100 year flux or, indeed, the limiting flux is not significantly larger than the 1 in 10 year flux. For example, at $L = 4.5$ the limiting flux is between 1.1 and 1.3 times larger than the 1 in 10 year flux. This is not the case when the fluxes are unbounded and the differences between the 1 in 10 and

1 in 100 year fluxes are much greater. For example, at $L = 6.5$ the 1 in 100 year fluxes of $E = 4.0$ and $E = 6.0$ MeV electrons are factors of 3.6 and 5.9 times higher than the corresponding 1 in 10 year events. A major consequence of this type of behavior is that there are a much larger number of occurrences of fluxes approaching the 1 in 100 year flux for the bounded compared to unbounded cases. This is demonstrated in Table 4 where we tabulate the number of times the daily average flux is within a factor of two of the corresponding 1 in 100 year flux. In the table the bounded cases are printed in bold, the undetermined case in italic and the unbounded cases in normal font. At $L = 4.5$, where the daily average $E = 1.0$ MeV fluxes are bounded, the daily average $E = 1.0$ MeV flux lies within a factor of two of the 1 in 100 year flux on 126 days. Further out, at $L = 6.5$, where the corresponding fluxes are unbounded, the daily average $E = 1.0$ MeV flux lies within a factor of two of the 1 in 100 year flux on only 12 days. Thus, the behavior of the tail of the distribution is important when not only determining the 1 in 100 year flux but also in determining the number of times the fluxes approach within a given factor of the 1 in 100 year flux.

It is informative to compare the results of our study with the IRENE AE9 radiation environment model (Johnston et al., 2014; O'Brien et al., 2018). Figure 10a shows a comparison between the 99th percentile of the BDD-IIR fluxes at $L = 4.25$ as a function of energy (red trace and symbols) with the 99th percentile of version 1.5 of the IRENE AE9 radiation environment model for equatorial MEO orbit at 20,200 km (black trace and symbols). The results are largely in extremely good agreement both in magnitude and spectral shape for a wide range of energies from 0.6 to 6.0 MeV. This also gives us confidence in the measured fluxes at higher energies, in particular, up to 6.0 MeV. A significant departure is seen at $E = 8.0$ MeV with the 99th percentile of the AE9 model being a factor of 8 times greater than the 99th percentile of the BDD-IIR fluxes. The fact that the observed fluxes are less than those in AE9 at $E = 8.0$ MeV suggests that the

issue is not associated with background counting issues in the BDD-IIR. It could be due to background counting issues in the data used to determine the AE9 model, especially given the fact that the gradient in the AE9 fluxes becomes less steep around 6.0 MeV. Alternatively, it could be due to the methods used to fit the data. Determining the reason warrants further investigation but is beyond the scope of the present study.

In 2017, we conducted an extreme value analysis using ~14 years of data from the Radiation Environment Monitor on board the INTEGRAL spacecraft (Meredith et al., 2017). The 1 in 100 year event at $L = 4.25$ ranged from $1.5 \times 10^7 \text{ cm}^{-2} \text{ s}^{-1} \text{ sr}^{-1} \text{ MeV}^{-1}$ at $E = 0.69$ MeV to $6.4 \times 10^5 \text{ cm}^{-2} \text{ s}^{-1} \text{ sr}^{-1} \text{ MeV}^{-1}$ at $E = 2.05$ MeV. These findings can be compared with the new results from the NS41 BDD-IIR instrument. The 1 in 100 year fluxes determined from the BDD-IIR data at $L = 4.25$ range from $1.2 \times 10^7 \text{ cm}^{-2} \text{ s}^{-1} \text{ sr}^{-1} \text{ MeV}^{-1}$ at $E = 0.6$ MeV to $3.0 \times 10^6 \text{ cm}^{-2} \text{ s}^{-1} \text{ sr}^{-1} \text{ MeV}^{-1}$ at $E = 2.0$ MeV (Figure 10b). The results are in good agreement at 0.8 and 1 MeV but the INTEGRAL results are about a factor of five lower at 1.6 and ~2 MeV.

One of the largest geomagnetic storms of the last 20 years was the Halloween storm in 2003, with a Dst minimum of -383 nT on 30th October at 22:00 UT. Following the storm a new outer radiation belt formed at low L , peaking in the slot region inside $L = 3.0$ (Baker et al., 2004; Horne et al., 2005). This event is not associated with large fluxes of relativistic electrons as observed by NS41, either toward the edge of the outer radiation belt or in the usual position of the heart of the radiation belt. This event serves to show that the 1 in 10 and 1 in 100 year fluxes in MEO and GEO are not related to the most extreme storms as monitored by the Dst index. This is consistent with Horne et al. (2018) who found that satellites at GEO are more likely to be at risk from a fast solar wind stream event than from a major storm. In such storms the outer radiation belt often reforms inside MEO and is depleted at higher L values. Relativistic electrons during this type of extreme storm would

not pose a risk to satellites in MEO or GEO. However, the situation would be different for satellites in the slot region, such as the O3B satellites. The slot region is usually devoid of relativistic electrons but, during such severe storms, can become elevated and remain elevated for weeks or even months (Baker et al., 2007), significantly increasing the risk to satellites operating in this region.

Conclusions

We have conducted an extreme value analysis of the relativistic electron flux in GPS orbit as a function of energy and L using data from the BDD-IIR instrument on the US NS41 satellite. Our principal results are as follows:

1. The 1 in 10 year flux at $L = 4.5$, near the heart of the outer radiation belt, decreases with increasing energy ranging from $8.2 \times 10^6 \text{ cm}^{-2} \text{ s}^{-1} \text{ sr}^{-1} \text{ MeV}^{-1}$ at $E = 0.6 \text{ MeV}$ to $33 \text{ cm}^{-2} \text{ s}^{-1} \text{ sr}^{-1} \text{ MeV}^{-1}$ at $E = 8.0 \text{ MeV}$. The 1 in 100 year event exhibits a similar trend, lying in the range $9.0 \times 10^6 \text{ cm}^{-2} \text{ s}^{-1} \text{ sr}^{-1} \text{ MeV}^{-1}$ – $56 \text{ cm}^{-2} \text{ s}^{-1} \text{ sr}^{-1} \text{ MeV}^{-1}$, and is a factor of 1.1–1.7 larger than the corresponding 1 in 10 year event.
2. The 1 in 10 year flux at $L = 6.5$, on field lines which map to the vicinity of geostationary orbit, decrease with increasing energy ranging from $6.2 \times 10^5 \text{ cm}^{-2} \text{ s}^{-1} \text{ sr}^{-1} \text{ MeV}^{-1}$ at $E = 0.6 \text{ MeV}$ to $0.48 \text{ cm}^{-2} \text{ s}^{-1} \text{ sr}^{-1} \text{ MeV}^{-1}$ at $E = 8.0 \text{ MeV}$. The 1 in 100 year event (red line) exhibits a similar trend, lying in the range $6.9 \times 10^5 \text{ cm}^{-2} \text{ s}^{-1} \text{ sr}^{-1} \text{ MeV}^{-1}$ – $6.0 \text{ cm}^{-2} \text{ s}^{-1} \text{ sr}^{-1} \text{ MeV}^{-1}$, and is a factor of 1.1–13 times larger than the corresponding 1 in 10 year event.
3. Our analysis suggests that the fluxes of relativistic electrons with energies in the range $0.6 < E < 2.0 \text{ MeV}$ in the region $4.25 < L < 4.75$ have an upper bound. In contrast, further out, in the region $5.5 \leq L \leq 7.0$, and at higher energies the fluxes of relativistic electrons are largely unbounded.

The 1 in N year electron fluxes determined here as a function of energy and L can serve as benchmarks against

which to compare other extreme space weather events and to help assess the potential impact of an extreme event.

Data availability statement

The data used in this study is publicly available from <http://www.ngdc.noaa.gov/stp/space-weather/satellite-data/satellite-systems/gps/data/ns41>. The solar wind data, geomagnetic activity indices and sunspot numbers are available from the NASA GSFC OMNI website (<https://omniweb.gsfc.nasa.gov/>). The results and data shown in this study can be downloaded from the UK Polar Data Centre (<https://doi.org/10.5285/30bba6e1-de1e-4ef9-97a6-d64e9eaca820>).

Acknowledgments

We would like to acknowledge the skill and attention to detail of Timothy J. Wehner that enabled these measurements at Medium Earth Orbit. We acknowledge Los Alamos National Laboratory for generating the BDD-IIR data products used in this study, and the National Oceanic and Atmospheric Administration's archive of the data files themselves.

The research leading to these results has received funding from the Natural Environment Research Council Grants NE/V00249X/1 (Sat-Risk) and NE/R016038/1. to satellites in MEO or GEO. However, the situation would be different for satellites in the slot region, such as the O3B satellites. The slot region is usually devoid of relativistic electrons but, during such severe storms, can become elevated and remain elevated for weeks or even months (Baker et al., 2007), significantly increasing the risk to satellites operating in this region.

References

Baker, D. N., Blake, J. B., Callis, L. B., Cummings, J. R., Hovestadt, D., Kanekal, S., et al. (1994). Relativistic electron acceleration and decay time

scales in the inner and outer radiation belts: SAMPEX. *Geophysical Research Letters*, 21(6), 409–412. <https://doi.org/10.1029/93GL03532>

Baker, D. N., Kanekal, S. G., Horne, R. B., Meredith, N. P., & Glauert, S. A. (2007). Low-altitude measurements of 2–6 MeV electron trapping lifetimes at $1.5 \leq L \leq 2.5$. *Geophysical Research Letters*, 34(20), L20110. <https://doi.org/10.1029/2007GL031007>

Baker, D. N., Kanekal, S. G., Li, X., Monk, S. P., Goldstein, J., & Burch, J. L. (2004). An extreme distortion of the Van Allen belt arising from the “Halloween” solar storm in 2003. *Nature*, 432(7019), 878–881. <https://doi.org/10.1038/nature03116>

Blake, J. B., Kolasinski, W. A., Fillius, R. W., & Mullen, E. G. (1992). Injection of electrons and protons with energies of tens of MeV into $L < 3$ on 24 March 1991. *Geophysical Research Letters*, 19(8), 821–824. <https://doi.org/10.1029/92GL00624>

Cayton, T. E., Belian, R. D., Gary, S. P., Fritz, T. A., & Baker, D. N. (1989). Energetic electron components at geosynchronous orbit. *Geophysical Research Letters*, 16(2), 147–150. <https://doi.org/10.1029/GL016i002p00147>

Cayton, T. E., Chen, Y., Friedel, R. H. W., & Kippen, R. M. (2010). *Analysis of electron and proton environmental data for medium Earth orbit (2000–present)*. Technical Report LA-UR-10-04234. Los Alamos National Laboratory.

Cayton, T. E., Drake, D. M., Spencer, K. M., Herrin, M., Wehner, T. J., & Reedy, R. C. (1998). *Description of the BDD-IIR: Electron and proton sensors on the GPS*. Technical Report LA-UR-98-1162. Los Alamos National Laboratory.

Coles, S. (2001). *An introduction to statistical modelling of extreme values*. Springer.

Della-Marta, P. M., Mathis, H., Frei, C., Liniger, M. A., Kleinn, J., & Appenzeller,

- C. (2009). The return period of wind storms over Europe. *International Journal of Climatology*, 29(3), 437–459. <https://doi.org/10.1002/joc.1794>
- Denton, M. H., & Cayton, T. E. (2011). Density and temperature of energetic electrons in the Earth's magnetotail derived from high-latitude GPS observations during the declining phase of the solar cycle. *Annales Geophysicae*, 29(10), 1755–1763. <https://doi.org/10.5194/angeo-29-1755-2011>
- Dey, A. K., & Das, K. P. (2016). Modeling extreme hurricane damage using the generalized Pareto distribution. *American Journal of Mathematical and Management Sciences*, 35(1), 55–66. <https://doi.org/10.1080/01966324.2015.1075926>
- Elvidge, S., & Angling, M. J. (2018). Using extreme value theory for determining the probability of Carrington-like solar flares. *Space Weather*, 16(4), 417–421. <https://doi.org/10.1002/2017SW001727>
- EUSPA EO and GNSS Market Report. (2022). Retrieved from https://www.euspa.europa.eu/sites/default/files/uploads/euspa_market_report_2022.pdf
- Frederickson, A. R., Mullen, E. G., Brautigam, D. H., Kerns, K. J., & Holman, E. G. (1991). Radiation induced insulator discharge pulses in the CRRES internal discharge monitor satellite experiment. *IEEE Transactions on Nuclear Science*, 38(6), 778–784. <https://doi.org/10.1109/23.124153>
- Hapgood, M., Angling, M. J., Attrill, G., Bisi, M., Cannon, P. S., Dyer, C., et al. (2021). Development of space weather reasonable worst-case scenarios for the UK National Risk Assessment. *Space Weather*, 19, <https://doi.org/10.1029/2020SW002593>
- HM Government, National Risk Register. (2020). Retrieved from <https://www.gov.uk/government/publications/national-risk-register-2020>
- Horne, R. B., Phillips, M. W., Glauert, S. A., Meredith, N. P., Hands, A. D. P., Ryden, K., & Li, W. (2018). Realistic worst case for a severe space weather event driven by a fast solar wind stream. *Space Weather*, 16(9), 1202–1215. <https://doi.org/10.1029/2018SW001948>
- Horne, R. B., Thorne, R. M., Shprits, Y. Y., Meredith, N. P., Glauert, S. A., Smith, A. J., et al. (2005). Wave acceleration of electrons in the Van Allen radiation belts. *Nature*, 437(7056), 227–230. <https://doi.org/10.1038/nature03939>
- Iucci, N., Levitin, A. E., Belov, A. V., Eroshenko, E. A., Pitsyn, N. G., Villoresi, G., et al. (2005). Space weather conditions and spacecraft anomalies in different orbits. *Space Weather*, 3(1), S01001. <https://doi.org/10.1029/2003SW000056>
- Johnston, W. R., O'Brien, T. P., Ginot, G. P., Huston, S. L., Guild, T. B., & Fennelly, J. A. (2014). AE9/AP9/SPM: New models for radiation belt and space plasma specification. *Proceedings of SPIE*, 9085.
- Koller, J., Chen, Y., Reeves, G. D., Friedel, R. H. W., Cayton, T. E., & Vrugt, J. A. (2007). Identifying the radiation belt source region by data assimilation. *Journal of Geophysical Research*, 112(A6), A06244. <https://doi.org/10.1029/2006JA012196>
- Koons, H. C., & Fennel, J. F. (2006). Space weather effects on communications satellites. *URSI Radio Science Bulletin*, 316, 27–41.
- Krausmann, E. (2011). The space-weather awareness dialogue: Findings and outlook. JRC Scientific and Technical Reports (pp. 25–26).
- Li, W., & Hudson, M. K. (2019). Earth's Van Allen radiation belts: From discovery to the Van Allen Probes era. *Journal of Geophysical Research: Space Physics*, 124(11), 8319–8351. <https://doi.org/10.1029/2018JA025940>
- Li, Y., Cai, W., & Campbell, E. P. (2005). Statistical modeling of extreme rainfall in southwest western Australia. *Journal of Climate*, 18(6), 852–863. <https://doi.org/10.1175/JCLI-3296.1>
- Meredith, N. P., Cain, M., Horne, R. B., Thorne, R. M., Summers, D., & Anderson, R. R. (2003). Evidence for chorus-driven electron acceleration to relativistic energies from a survey of geomagnetically disturbed periods. *Journal of Geophysical Research*, 108(A6), 1248. <https://doi.org/10.1029/2002JA009764>
- Meredith, N. P., Horne, R. B., Isles, J. D., & Green, J. C. (2016a). Extreme energetic electron fluxes in low Earth orbit: Analysis of POES $E > 30$, $E > 100$ and $E > 300$ keV electrons. *Space Weather*, 14(2), 136–150. <https://doi.org/10.1002/2015SW001348>
- Meredith, N. P., Horne, R. B., Isles, J. D., & Rodriguez, J. V. (2015). Extreme relativistic electron fluxes at geosynchronous orbit: Analysis of GOES $E > 2$ MeV electrons. *Space Weather*, 13(3), 170–184. <https://doi.org/10.1002/2014SW001143>
- Meredith, N. P., Horne, R. B., Isles, J. D., Ryden, K. A., Hands, A. D. P., & Heynderickx, D. (2016b). Extreme internal charging currents in medium Earth orbit: Analysis of SURF plate currents on Giove-A. *Space Weather*, 14(8), 57–591. <https://doi.org/10.1002/2016SW001404>
- Meredith, N. P., Horne, R. B., Sandberg, I., Papadimitriou, C., & Evans, H. D. R. (2017). Extreme relativistic electron fluxes in the Earth's outer radiation belt: Analysis of INTEGRAL IREM data. *Space Weather*, 15(7), 917–933. <https://doi.org/10.1002/2017SW001651>
- Messenger, S. R., Jackson, E. M., Warner, J. H., Walters, R. J., Cayton, T. E., Chen, Y., et al. (2011). Correlation of telemetered solar array data with particle detector data on GPS spacecraft. *IEEE Transactions on Nuclear Science*, 58(6), 3118–3125. <https://doi.org/10.1109/TNS.2011.2172957>

- Nogaj, M., Yiou, P., Parey, S., Malek, F., & Naveau, P. (2006). Amplitude and frequency of temperature extremes over the North Atlantic region. *Geophysical Research Letters*, 33(10), L10801. <https://doi.org/10.1029/2005GL024251>
- O'Brien, T. P., Johnston, W. R., Huston, S. L., Roth, C. J., Guild, T. B., Su, Y.-J., & Quinn, R. A. (2018). Changes in AE8/AP9-IRENE version 1.5. *IEEE Transactions on Nuclear Science*, 65(1), 462–466. <https://doi.org/10.1109/TNS.2017.2771324>
- Olson, W. P., & Pfizter, K. (1977). *Magnetospheric magnetic field modelling annual scientific report*. Air Force Office of Scientific Research.
- Picklands, J. (1975). Statistical inference using extreme order statistics. *Annals of Statistics*, 3, 119–131.
- Pierrard, V., & Lemaire, J. (1996). Fitting AE8 energy spectra with two Maxwellian functions. *Radiation Measurements*, 26(3), 333–337. [https://doi.org/10.1016/1350-4487\(96\)00057-1](https://doi.org/10.1016/1350-4487(96)00057-1)
- R Development Core Team. (2008). *R: A language and environment for statistical computing*. R Foundation for Statistical Computing. ISBN 3-900051-07-0 Retrieved from <http://www.R-project.org>
- Reagan, J. B., Nightingale, R. W., Gaines, E. E., Imhof, W. L., & Stassinopoulos, E. G. (1981). Outer zone energetic electron spectral measurements. *Journal of Spacecraft and Rockets*, 18(1), 83–88. <https://doi.org/10.2514/3.57791>
- Reeves, G. D., Chen, Y., Cunningham, G. S., Friedel, R. W. H., Henderson, M. G., Jordanova, V. K., et al. (2012). Dynamic radiation environment assimilation model: DREAM. *Space Weather*, 10(3), S03006. <https://doi.org/10.1029/2011SW000729>
- Rodgers, D. J., & Ryden, K. A. (2001). Internal charging in space. In R. A. Harris & (Eds.), *Proceedings of 7th spacecraft charging technology conference, Noordwijk, The Netherlands, 23–27 April, ESA SP-476* (p. 25). European Space Agency.
- Satellite Industry Association. (2022). State of the satellite industry report 2022. Retrieved from <https://sia.org/news-resources/state-of-the-satellite-industry-report>
- Shprits, Y., Subbotin, D., Ni, B., Horne, R., Baker, D., & Cruce, P. (2011). Profound change of the near-Earth radiation environment caused by solar superstorms. *Space Weather*, 9(8), S08007. <https://doi.org/10.1029/2011SW000662>
- Shprits, Y. Y., Elkington, S. R., Meredith, N. P., & Subbotin, D. A. (2008). Review of modeling of losses and sources of relativistic electrons in the outer radiation belt I: Radial transport. *Journal of Atmospheric and Solar-Terrestrial Physics*, 70(14), 1679–1693. <https://doi.org/10.1016/j.jastp.2008.06.008>
- Shprits, Y. Y., Subbotin, D. A., Meredith, N. P., & Elkington, S. R. (2008). Review of modeling of losses and sources of relativistic electrons in the outer radiation belt II: Local acceleration and loss. *Journal of Atmospheric and Solar-Terrestrial Physics*, 70(14), 1694–1713. <https://doi.org/10.1016/j.jastp.2008.06.014>
- Tibaldi, C. B., Strauss, H., & Zervas, C. E. (2012). Modelling sea level rise impacts on storm surges along U.S. coasts. *Environmental Research Letters*, 7(1), 14032. <https://doi.org/10.1088/1748-9326/7/1/014032>
- Thomson, A. W. P., Dawson, E. B., & Reay, S. J. (2011). Quantifying extreme behavior in geomagnetic activity. *Space Weather*, 9(10), S10001. <https://doi.org/10.1029/2011SW000696>
- Thorne, R. M. (2010). Radiation belt dynamics: The importance of wave-particle interactions. *Geophysical Research Letters*, 37(22), L22107. <https://doi.org/10.1029/2010GL044990>
- Tsubouchi, K., & Omura, Y. (2007). Long-term occurrence probabilities of intense geomagnetic storm events. *Space Weather*, 5(12), S12003. <https://doi.org/10.1029/2007SW000329>
- Tuszewski, M., Cayton, T. E., & Ingraham, J. C. (2002). A new numerical technique to design satellite energetic electron detectors. *Nuclear Instruments & Methods in Physics Research, Section A*, 482(3), 653–666. [https://doi.org/10.1016/S0168-9002\(01\)01735-1](https://doi.org/10.1016/S0168-9002(01)01735-1)
- US Space Weather Benchmarks Phase 1 Report. (2018). Retrieved from <https://www.sworm.gov/publications/2018/Space-Weather-Phase-1-Benchmarks-Report.pdf>
- Varotsou, A., Friedel, R. H., Reeves, G. D., Lavraud, B., Skoug, R. M., Cayton, T. E., & Bourdarie, S. (2008). Characterization of relativistic electron flux rise times during the recovery phase of geomagnetic storms as measured by the NA41 GPS satellite. *Journal of Atmospheric and Solar-Terrestrial Physics*, 70(14), 1745–1759. <https://doi.org/10.1016/j.jastp.2008.01.020>
- Webb, F. D., & Allen, J. H. (2004). Spacecraft and ground anomalies related to the October–November 2003 solar activity. *Space Weather*, 2(3), S03008. <https://doi.org/10.1029/2004SW000075>
- Wrenn, G. L., Rodgers, D. J., & Ryden, K. A. (2002). A solar cycle of spacecraft anomalies due to internal charging. *Annales Geophysicae*, 20(7), 953–956. <https://doi.org/10.5194/angeo-20-953-2002>
- The paper originally published in Space Weather, 21 is republished with authors' permission.*

© 2023. The Authors.

This is an open access article under the terms of the Creative Commons Attribution License, which permits use, distribution and reproduction in any medium, provided the original work is properly cited. 

The investment case for land tenure security in Sub-Saharan Africa: A cost-benefit analysis

Land tenure security is a critical government service that has repercussions on agricultural productivity, housing development, business investment, and the development of urban areas. The present study presents a cost-benefit analysis of tenure security in Sub-Saharan Africa. Readers may recall that we published the first part of the study in September 2023 issue of *Coordinates*. The first part focussed on the cost factor and this part focusses on the benefit analysis

Frank F.K. Byamugisha
Independent Consultant

Nancy Dubosse
Copenhagen Consensus Center,
Tewksbury, MA, USA

Benefits

The observed benefits of land registration vary depending on whether the intervention takes place in rural or urban areas. Annexes 1 and 2 summarize the evidence in the literature on rural and urban tenure security interventions.

Benefits of improved rural tenure security

With respect to land registration in rural areas, there is a narrow range of impacts observed and measured. The anticipated benefits include an (a) increase in farmers' demand for farm improvements, productive and land conservation technologies, a consequence of improved confidence of being in possession of the parcel in the long run; (b) increase in the supply of formal credit through the creation of tradable collaterals; and (c) as a result of either or both of the preceding benefits, an increase in yields and income.

Successful country examples of rural land tenure interventions include the national land certification and registration programs in Vietnam, Rwanda and Ethiopia. In the former, land titling results, on average, in a 7.5% increase in the cultivation of perennial crops and a reallocation of 11–12 weeks of nonfarm labor time by the household (Do and Iyer 2007). In Rwanda,

households affected by land tenure were almost 10 percentage points more likely to make or maintain soil conservation investments in structures such as bunds, terraces and check dams, which was double the change in investment in the control group (Ngoga, 2019). There is also the case of Benin, which in the context of customary tenure, demonstrated that treatment households are 39% to 43% more likely to grow perennial cash crops and invest in trees on their parcels (Wren-Lewis, Becerra-Valbuena and Hounghbedji 2020). Korsaga (2018) evaluates the impact of land security tenure on technical efficiency of 706 villages across 45 provinces in Burkina Faso. Farmers with land tenure security are more efficient in their use of inputs than are farmers with unsecured farms. The difference in technical efficiency between two groups was low (0.029) but significant at 1%.

However, there are studies that show limited or no impact of tenure security on agricultural productivity or household welfare evidence. Alban Singirankabo and Ersten (2020) found, after reviewing 85 studies, that in 34% of studies, land rights were not found to be a significant factor in determining whether farmers made land-improving investments, used yield-enhancing inputs, accessed credit, or improved the productivity of land. Other country cases that also reveal less than spectacular results of

land titling on agricultural productivity, credit or migration include Ahn (2019) for Cambodia; Aikielli and Markussen (2017) for Tanzania; Huntington and Shenoy (2021) for Zambia, and Coulibaly Sagoe, and Shixiang (2021) for Mali.

Huntington and Shenoy (2021) undertook a randomized trial in Zambia in which customary land certificates were issued at the end of a process that included sensitization, the formation of a village land committee, and training in land management and conflict resolution. One treatment arm was also the beneficiary of agroforestry extension. These certificates were signed by the chief and confirmed in writing the right to use the land in perpetuity. The parcels could not be sold or transferred except through inheritance. The researchers found a statistically significant 3 percentage point increase in agroforestry at the household-level from the treatment arm that was exposed to both interventions. Looking at over 3000 large Zambian farms, Ali and Deininger (2021) also find no impact of de jure certification on productivity as measured by gross profit per ha. They conclude, also noting Huntington and Shenoy's (2021) findings, that the reason for this finding is that user rights granted by chiefs are not legally recognized, nor can they be collateralized. In Zambia, the only way to have land rights formally documented is to convert customary land to 'state land'. Since 1995, more than 30 million hectares have been transferred to the State.

Key to the notion of tenure security is the transferability and collateralization of parcels. A similar occurrence was observed in China. Following a national initiative to improve land tenure security in 2009, there remained suppressed farmer investment even though farmers held 30-year use rights to land. They were subsequently granted the right to transfer, and a subset of counties officially recognized farm user certificates as a form of collateral. These households were 9.1 percentage points more likely to receive a loan. Whereas in the other counties that had titles but no official recognition of them as collateral, there was a 5.5 percentage

point increase in unmet demand for credit. Low productivity was ameliorated by letting small-holder farmers transfer farmland to others for agricultural production and use the certificates as collateral (Li, Zhang, and Hayes 2018; Cheng, Zhou, and Zhang 2021).

Another randomized trial of a land formalization program was in Benin, which involved raising awareness about the demarcation and documentation of parcel boundaries. The issuance of certificates was not part of the treatment, but owners had the expectation of receipt from authorities. Treated parcels were 2.4 percentage points more likely than control parcels to be used primarily for perennial crops, and they are 1.7 percentage points more likely to have a newly planted tree.

These two experiments share a common finding of statistically significant farm investment, evidenced by increased use of fertilizer, improved seeds, labor time, and/or the decision to plant perennial crops. Other studies demonstrating this outcome include Deininger et al. (2021) for Malawi, Abera and Chemin (2021) for Kenya; Hayes, Roth, and Zepeda (1997) for Gambia, and Do and Iyer (2007) for Vietnam. Perennial and annual crops do not generate similar income streams. While the payback period for the latter is at least 1 year, it takes 3 years for a cocoa tree to start bearing fruit and an additional 6–7 years to reach full maturity and its highest yield, which may last for at least 10 years (Bros et al. 2019).

Identification of the impacts of tenure security depends greatly on the timing of data collection and the context in which the intervention is applied. Goldstein et al. (2018) conclude that it is generally difficult to observe increases in agricultural productivity because it takes more than one year for investments in perennial crops to generate productivity gains; a notion supported by Higgins et al. (2018), who, after investigating 59 studies, found strong support for productive or commercial investment by farmers, but no change in productivity or income. Thus, farm investment may be the channel

through which higher productivity and thus incomes are realized.

A specific example of this is Vietnam where land reform led to a statistically significant increase in the proportion of total cultivated area devoted to multi-year crops: households in provinces that had completed land certification increased their proportion by 7.5 percentage points over the period 1993–98. Households also increased non-farm activity by 2.7 weeks per working member between 1992–93 and 1997–98, the most reported activities being sales in markets, food processing, woodworking, and work in the textiles and garment industry. This corresponds to an increase of between 11 and 12 weeks worked in the nonfarm sector for the household, as the average number of working members in the household was 4.37 in 1992–93 and 4.46 in 1997–98. Do and Iyer (2007) concluded that while they found no significant impact on overall household consumption expenditure or agricultural income at the time of analysis, the increases in investment were likely to yield greater returns in the future.

For the purposes of this cost-benefit analysis, the benefit of rural land tenure security is largely based on a meta-analysis by Lawry et al. (2016), which was limited to lower-income and lower-middle-income countries.

- Eight of the 20 cases (two in Africa) reveal that there was an average increase of 42% on the monetary value of agricultural productivity; however, the prediction interval (the distribution of effects in the true population) includes zero, albeit in the far-left tail. The two lowest mean effects (less than 25%) are attributed to Ethiopia and Madagascar, and the study of the former includes zero in its mean confidence interval at 95%.
- The ten studies used, including five African countries, show evidence of an increase in the probability of farmer investment by 5 percentage points, but the prediction interval also includes zero. Again, this includes both Ethiopia and Madagascar, as

was also the case for China, although the study used was before the transferability and collateralization of land mentioned above.

- Four of the cases (Nicaragua, Peru, India, and Vietnam) show evidence of a 15% increase in household income. Heterogeneity is low, and the prediction interval is positive; however, there are no African countries included in the sample.

The wide dispersion observed for both agricultural productivity and farm investment is critical because the authors demonstrate that the effects for the Sub-Saharan African countries were markedly lower. Using eight publications involving Sub-Saharan African countries⁴, the authors conducted a formal moderator analysis for effects on productivity and long-term investment in the region. Effects sizes are significantly lower for agricultural productivity; the mean effect is below zero (-0.42; p-value 0.01). The coefficient for farm investment was not statistically significant, and there was not enough evidence to calculate a mean effect for household income.

Lawry et al. (2016) also conducted an assessment of seven qualitative studies carried out in Sub-Saharan Africa, a study focused on Peru, and one on Vietnam. While there was significant variation, there were almost exclusively positive experiences regarding investment, long-term production, leasing out land and consumption.

Since the systematic review of Lawry et al. (2016), additional evidence has emerged. In a more recent systematic review, Higgins et al. (2018) investigate the impact of tenure security in 59 low- and middle- income countries (25 on Sub-Saharan African countries), and found that there is strong support that land tenure security increases productive and commercial investment, for which it is assumed that higher income will be realized in the future. Table 6 lists the most recent evidence of tenure security intervention impacts in sub-Saharan Africa.

Although the channels vary, it can be concluded that household welfare improves in the medium to long term as a result of improved land tenure security and the subsequent investments made by farmers. The rights to transfer, exchange and lease land-user certificates create a formal market for land, which may achieve a better allocation of land than a centralized/informal system. The right to mortgage land-user certificates allows farmers to undertake investments that have high up-front costs, such as planting multi-year crops (Do and Iyer 2007).

Some country examples include the following:

- Deininger et al. (2021) reveal that the right to bequeath or sell land in Malawi is estimated to significantly increase the likelihood of long-term investment via organic manure application by 0.12 and 0.07 percentage points, respectively.
- Muchomba (2017) examines household consumption patterns in the Tigray region of Ethiopia after a land-certification exercise that provided households with the right to use, lease, and bequeath land to family members. Monthly expenditures on healthcare increased by 33% after joint certification (p-value .01); the consumption of homegrown food increased by 57% (p-value 0.10); consumption of clothing increased by 36.9% (p-value 0.10), and investment in education increased by 59.9% (p-value 0.01).
- In Kenya, tenure security increased the proportion of people borrowing by 9 percentage points. People who borrowed from a credit union indicated that the loans are not only used for agriculture: 26% report using the

loan for human capital investment, 23% for business investment, and 22% for health-related expenses. The main source of collateral for these credit union loans is the harvest. Aberra and Chemin (2021) conclude that increased security of property rights is used as collateral to obtain loans and is used for more general purposes than just agriculture.

- In Ethiopia, Ayalew, Admasu, and Chamberlin (2021) observe a significant welfare difference between treated and control groups and note that rental market participation and hired labor are the main channels through which certification affects household consumption. Average treated households used around 19.15 more hours of hired labor and spent 75.8 hours more on soil conservation.

To summarize, the bulk of studies on Sub-Saharan Africa find modest to no impact on agricultural productivity and household income but do demonstrate substantive evidence of farmer investment in its various forms. Given the body of evidence around farm investment in African countries and the increase in household income and consumption in non-African countries (but also low-income) as a result of farmer investment, we therefore use the central income estimate of 15%, established by the results of Lawry et al. (2016). This increased welfare could come from expanded farm area or from non-farm activities like investment in livestock or agroforestry (see Table 6). Noting that impacts in Sub-Saharan Africa tend to be more modest and that the studies in Lawry et al. (2016) demonstrating household wealth benefits had a minimum of 5 years between initiation and assessment, we delay benefits for the first five years of the intervention period.

Benefit-cost ratio, rural land tenure

According to the World Bank's Open Data, the value added from Agriculture, Forestry, and Fishing to GDP of Sub-Saharan Africa in 2020 was approximately

Table 6: Impact of Increased Rural Land Tenure Security from Lawry et al. (2016)

Impact area	Mean effect size (95% confidence interval)
Agricultural productivity	0.42 (0.23–0.61)
Farm investment probability	0.05 (0.01–0.09)
Household income	0.15 (0.06–0.24)

Note: Authors' estimation of confidence interval is based on results published in Lawry et al. (2016) and not on the source data.

Table 7: Recent Evidence of Impact of Land Tenure Interventions in Sub-Saharan Africa Post Lawry et al. (2017)

COUNTRY	Impact area			Reference
	Agricultural productivity	Farm investment	Household consumption, welfare	
BENIN	+2.4 percentage point, perennial crops	+1.7 percentage point trees		Goldstein et al. (2018)
ZAMBIA		+3%, agroforestry		Huntington and Shenoy (2021)
BENIN		600 ha extra tree cover		Wren-Lewis et al. 2020
RWANDA			+USD 2.6 billion mortgage lending (65% secured with residential, 30% with agricultural, and 5% with commercial land)	Ali, Deininger, and Duponchel (2016)
BURKINA FASO	30.8% more productive			Coulibaly (2021)
CAMEROON	+ FCFA 207,881 per hectare (p-value .01)			Joel and Bergaly (2020)
RWANDA	+217.79 kg/ha maize yields (p-value .01)			Ngango and Hong (2021)
MALAWI	+17% Cash crop production (p-value 5%) with the right to bequeath land granted to men	+13 % fertilizer application by women (p-value 1%); +24% when women granted right to sell (5% significance)		Deininger et al. (2021)
ETHIOPIA			+33% (p-value 1%) increase in monthly healthcare expenditures; +59.9% increase in education (p-value 1%)	Muchomba (2017)
KENYA		+15% (4.5 days more labor time (p-value 1%))	+ 56% increase in borrowing (p-value .05)	Aberra and Chemin (2021)
ETHIOPIA			+28% per capita consumption	Ayalew, Admasu, and Chamberlin (2021)

US\$ 342.9 billion. Assuming that 84% of rural areas are characterized by unregistered land parcels, the value added of this subregion is US\$ 287.7 billion.

The number of households treated by the intervention is approximately 83 million, with a starting point household income of US\$ 3461, on average. The benefits of tenure security are assumed to be enjoyed over a span of 30 years, and Agricultural GDP increases at an annual rate of 3.3% over that period, the average from 2011–2020.

The 15% wealth effect and an annual household uptake rate of 10% is applied starting in Year 6⁶; household income at this point is US\$ 4075. Afterwards 100% of the benefit is assessed until Year 30, at which point it is assumed that there is an increase in uncertainty, which could arise from several sources: radical political movements, the death of the original beneficiary and intergenerational transfer, among other things. The net present value (8%) of the benefits stream is US\$ 395.7 billion, and the

net present value (8%) of costs, which run over 10 years, is just under US\$ 21.7 billion. Thus, the benefit-cost ratio is 18.

Benefits of improved urban tenure security

Regarding the benefits of urban tenure security (Annex 2), by far the most common and consistent benefit is the increase in land values, which appears to concentrate around the value of 25% when outliers Indonesia (45%) and Cambodia (66%) are removed. This was the case in Peru, Ecuador, Philippines, and Tanzania. Durand-Lasserre et al. (2007) find considerable support for the claim that urban land titling increases property values: they observe that price increases of 25% are common following the provision of land titles.

Benefit-cost ratio, urban

The monetized benefit is a 25% level increase in housing values, realized in the year following registration and

is assumed to be preserved over the duration of the intervention period.

Average national housing prices were taken from the Center for Affordable Housing Finance in Africa, which posts the prices in purchasing power parity (PPP) dollars \$ (2020), for the 20 largest Sub-Saharan African countries by population. The inflation adjusted average housing price in 2020 is US\$ 41,845. The net present value (8%) of the benefits stream is US\$ 236.9 billion. Again, with the net present value of costs being US\$ 5.3 billion, the benefit-cost ratio is 45.

When weighted by the proportion of urban residents of total population, the average housing price is US\$ 28,240. Here, the net present value (8%) of the benefits stream is US\$ 159.9 billion, yielding a benefit-cost ratio of 30.

Conclusion

The summary of the benefit-cost analysis can be found in Table 7.

Previous cost-benefit analyses of land tenure security interventions by the Copenhagen Consensus Center yielded similar good results. In Ghana, the central benefit-cost ratio of a national land titling program, which covered 75% of land in both rural and urban areas was 91, ranging from 5 to 219 depending on various scenarios (Adjasi et al. 2020). In Malawi, for a similar country-wide titling intervention, the BCR ranged from 18 to 138, with a central estimate of 73 (National Planning Commission, 2021).

Although not included in the calculations for both urban and rural land titling programs, there are efficiency gains in modernizing land administration services. Technical (e.g., digitization) and managerial innovations can create efficiencies and improve workflow, thereby reducing the costs (direct and indirect) of registering land transactions. In Lesotho, the total days required to register property declined from 101 to 43 following regulatory reform. In Jamaica, institutional and administration reforms reduced property registration and transfer times from 70 to 30 and 25 to 5 days, respectively, while reducing survey check times from 182 to 35 days (Millennium Challenge Corporation 2019). Ghana reduced the number of days to transfer property from 169 in 2005 to 34 in 2011; Uganda reduced the number of days to transfer property from 227 in 2007 to 48 in 2011. In Madagascar, titles, which involved 24 steps and took up to 6 years at a cost of US\$ 500 per title, reduced to US\$ 14 per title and a processing time of six months (Byamugisha 2013).

Critical success factors

- The cost of parcel registration and subsequent land transactions borne by the private sector is a critical determinant of the program’s success. Ali et al. (2021) found that despite a desire for formalization, 87% of rural land transactions in Rwanda remain informal because the cost of registration is higher than the willingness to pay. The authors estimate the willingness to pay at about 2% of the land’s value. Reforms to increase compliance by

reducing rural fees to affordable levels (including a waiver for the poor) would be revenue-neutral but greatly enhance social welfare. According to the World Bank’s 2019 Ease of Doing Business Survey, the cost of property registration in Sub-Saharan Africa is currently 10% of property value.

- According to Higgins et al. (2018), attention must be given to the potential exclusion that can result from securitization of land. Certain groups were found to have been blocked or hindered from benefiting from land formalization for a variety of reasons but mainly due to local institutions tasked with implementing the intervention doing so unfairly, with common instances of corruption, elite capture and clientelism leading to poorer households and women being unable to benefit from these interventions.
- There is also the challenge of sufficient funds allocated to capacity-building and implementation. The authority and power of local chiefs to govern land has been diluted by the incorporation of their powers into statutory law. Creation of ‘new’ institutions to support land governance creates new checks and balances on their authority in ways that did not exist before. This is an extension of state power into areas where it had limited influence. In reality, however, a lack of state capacity to follow through on this statutory influence implies that by default customary institutions have continued to dispense local justice and resolve conflicts over land just like before (Chimhowu 2019). This should also include reinforcement of the legal system, as the inability to enforce contracts and secure property rights could erode all anticipated benefits (Aberra and Chemin 2021). The authors undertook a randomized intervention in Kenya offering the services of a free lawyer for 2 years

(85% uptake in the treatment group) in a rural setting with prohibitive lawyer fees and numerous land disputes. Not all cases were fully resolved after two years, but legal representation increased the security of property rights, which translated into greater investment and access to credit. Two years after the start of the intervention, treated households had increased the number of days worked on their plot by 15% compared to control households. Investment increased by 21%. Access to credit to finance long-run productive investments (set up a business or agricultural and human capital investment) increased by 56% in the treatment versus the control group. Agricultural production increased by 42%.

Land titling and supportive investments to improve land administration is complex, involving many stakeholders. While the monetary costs are low if implemented efficiently and the benefits, at least to urban land titling, extraordinarily high, implementing a streamlined low-cost process to register land will reduce rents to some groups (such as surveyors), who benefit from current regulations that impede low-cost systematic process and reduce opportunities for land-related corruption. In many African countries, legacy titles will also have to be addressed. To initiate such a process, regulatory changes are a precondition; otherwise, reforms will not be sustainable. Furthermore, high level commitment to reform and detailed monitoring of implementation will be essential, and this should be highlighted.

Given the difference in benefit-cost ratios between urban and rural land and the need for regulatory changes to facilitate implementation, it may make sense to suggest adoption of a sequenced approach

Table 8: Summary Results of Benefit-Cost Analysis (US\$ billion)

Region	Benefits	Costs	Benefit-cost ratio (BCR)
Rural	395.71	21.72	18
Urban average	236.93	5.29	45
Urban weighted average	159.89		30

Annex 1: Principal Benefits of Rural Land Tenure Interventions

COUNTRY	Farmer investment, agricultural productivity	Access to credit	Agroforestry	Household consumption, income, welfare	Source
MADAGASCAR	Yields +7.2%; net revenue + 6.9%			Titled plots found 6% more valuable than untitled plots	Jacoby and Minten (2007)
THAILAND				Crop value per unit of land was higher by 12% to 26%	Feder Onchan, and Hongladarom (1987)
CHINA:		9.1 percentage points, where supported by regulatory framework that allows for land collateralization.			Cheng , Zhou, and Zhang (2021)
INDIA (Karnataka)	Productivity +8%; area under cultivation (cotton) +11% replacing rice.	13% more likely to receive crop loans		household consumption per capita + 8%; profits +12% increase in profits;	Subramanian and Kumar (2019)
ETHIOPIA	Productivity +45% (Holden Deininger and Ghebru 2009)			Land rented out +9 percentage points	Deininger and Feder (2009)
ETHIOPIA				prevalence of severe undernourishment 81% to 49%; poverty head count ratio 90% to 65%; 1 extra year of land certificate ownership increased food availability by 3.1%	Ghebru and Holden (2013)
GAMBIA	11.5% more likely to invest in well/fence		+21.2%		Hayes , Zhou, and Zhang (1997)
VIETNAM	+7.5% perennial crops			+11-12 weeks non-farm work	Do and Iyer (2007)

Annex 2: Principal Benefits Observed for Urban Land Titling

COUNTRY	Housing investment	Property value, post-title sale	Access to credit	Labor supply	Source
Buenos Aires, ARGENTINA	37% increase in overall housing improvement; walls +40%; roofs +48%				Galiani and Scharfrodsky, (2010); Whitney Cameron and Winters (2018)
BRAZIL			+25 percentage points		Piza, José, and Moura (2011)
PERU	+ 60% (Collier et al. 2019)	Land values + 20% to 30%; land market transactions +134% between 1999 and 2003 (Collier et al. 2019)		+12.2 hours/week after 2 years of formal property rights; +32 hours/week after 4 years	Field (2011)
ECUADOR		property value +23.5%			Lanjouw and Levy (2002)
PERU		+25%			Cuantarias and Delgado (2004)
Jakarta, INDONESIA		+45%			Durand-Lasserve et al. (2007)
Manila, PHILIPPINES		+25% (Durand-Lasserve et al. 2007). House prices +58%; rents +18% (Byamugisha 2013)			
CAMBODIA		+66%			Durand-Lasserve et al. (2007); Deutsch (2006)
TANZANIA		+26.9%			Aikieli and Markussen (2017)
MONGOLIA		Land value per square meter + 9,140 MNT vs. 4,450 MNT in the control areas.	+ 8% vs. 4% in control		Millennium Challenge Corporation (2021x)
Matero and George, ZAMBIA		+44%			Muyeba (2018)

at country level. Phase I would consist of registration of all urban land outside of slum areas (the scope involved can easily be quantified using satellite imagery, as was done in Nigeria) as well as elaboration of the regulatory framework for Phase II (area-based adjudication of all rural land at village/ community level together with definition of processes for rural-urban land conversion and village-wide issuance of titles where appropriate), to be followed by actual implementation of Phase II.

End notes

¹ The five countries surveyed in 2010/11 are Malawi, Niger, Nigeria, Tanzania and Uganda; the sixth country, surveyed in 2011/12, is Ethiopia.

² We estimate that only 30 out of 48 Sub-Saharan Africa countries would require special interventions to register communal land rights.

³ The percentage of urban population living in slums in Vietnam, China, South Africa and Rwanda in 2018 was 14, 25, 26, 30 and 42, respectively (World Bank Open Data, accessed January 2022).

⁴ Based on five-year average of U.S. consumer price inflation, 2017-2021 (World Bank Open Data).

⁵ The sample included four studies on Ethiopia and one each for Madagascar, Malawi, Rwanda and Zambia.

⁶ The delay of the benefits reflects the fact the household wealth impacts are observed in the medium-term, rather than as an immediate consequence.

References

Aberra, A. and M. Chemin. 2021. "Does Legal Representation Increase Investment? Evidence from a Field Experiment in Kenya." *Journal of Development Economics* 150: 102612. <https://doi.org/10.1016/j.jdevco.2020.102612>

Adjasi, C., S. Adiaba, S. RAZvi, and B. Wong. 2020. *Cost-Benefit Analysis of Land Title Reforms in Ghana: An Order of Magnitude Estimate, Ghana Priorities*. Copenhagen Consensus Center License: Creative Commons Attribution CC BY 4.0. https://www.copenhagenconsensus.com/sites/default/files/gp_a4_land.pdf

Ahn, J. 2019. *Two Essays on Farm Productivity in Rural Cambodia: Low Rice Yield in Tonle Sap Zone and Effects of Land Titling*. Seoul National University. <https://s-space.snu.ac.kr/bitstream/10371/150897/1/000000154624.pdf>

Aikaeli, J. & Markussen, T. (2017) The effects of land titling in Tanzania. WIDER Working Paper 2017/168. Helsinki: UNU-WIDER. <https://doi.org/10.35188/UNU-WIDER/2017/394-3>

Alban Singirankabo, U., & Willem Ertzen, M. (2020). Relations between Land Tenure Security and Agricultural Productivity: Exploring the Effect of Land Registration. *Land*, 9(5), 138. <https://doi.org/10.3390/land9050138>

Alden Wily, L. (2018). Collective Land Ownership in the 21st Century: Overview of Global Trends. *Land*, 7(2), 68. <https://doi.org/10.3390/land7020068>

Alden Wily, L. (2003). *Governance And Land Relations: A Review Of Decentralisation Of Land Administration And Management In AFRICA*. International Institute for Environment and Development.

Ali, D. A., & Deininger, K. (2021). *Does title increase large farm productivity? Institutional determinants of large land-based investments' performance in Zambia* (Policy Research Working Paper No. 9702). Development Research Group, World Bank. <https://openknowledge.worldbank.org/bitstream/handle/10986/35822/Does-Title-Increase-Large-Farm-Productivity-Institutional-Determinants-of-Large-Land-Based-Investments-Performance-in-Zambia.pdf?sequence=6&isAllowed=y>

Ali, D. A., Deininger, K., Mahofa, G., & Nyakulama, R. (2021). Sustaining land registration benefits by addressing the challenges of reversion to informality in Rwanda. *Land Use Policy*, 110, 104317. <https://doi.org/10.1016/j.landusepol.2019.104317>

Ali, D. A., K. Deininger, and M. Duponchel. 2016. *Using Administrative Data to Assess the Impact and Sustainability of Rwanda's Land Tenure Regularization*. World Bank, Policy Research Working Paper 7705, June. Washington, D.C.: World Bank.

Ali, D. A., K. Deininger, and M. Goldstein, M. 2011. *Environmental and Gender Impacts of Land Tenure Regularization in Africa*. Washington D.C.: World Bank. <https://openknowledge.worldbank.org/handle/10986/25527>

Ayalew, H., Y. Admasu, and J. Chamberlin. 2021. "Is Land Certification Pro-Poor? Evidence from Ethiopia." *Land Use Policy* 107: 105483. <https://doi.org/10.1016/j.landusepol.2021.105483>

Bah, Eh.M., Faye, I., Geh, Z.F. (2018). Unlocking Land Markets and Infrastructure Provision. In: Housing Market Dynamics in Africa. Palgrave Macmillan, London. https://doi.org/10.1057/978-1-137-59792-2_4

Bambio, Y., & Bouayad Agha, S. (2018). Land tenure security and investment: Does strength of land right really matter in rural Burkina Faso? *World Development*, 111, 130–147. <https://doi.org/10.1016/j.worlddev.2018.06.026>

Bandiera, P. (2010). Evaluating land administration systems: a comparative method with an application to Peru and Honduras, *Land Use Policy*, April 2010, DOI: 10.1016/j.landusepol.2009.04.005

Barnes, G., M. Digiano, and X. Augustinus. 2015. *Integrating Communal and Individual Property Rights: Learning from the Mexican Experience*. 2015 World Bank Conference on Land and Poverty. <https://www.oicrf.org/documents/40950/43224/Integrating+Communal+>

- and+Individual+Property+Rights+ Learning+from+the+Mexican+Ejido +Experience.pdf/8f7605a4-7250-2d6e-dcec-7a2a70f9fb32
- Bros, C., Desdoigts, A., & Kouadio, H. (2019). Land Tenure Insecurity as an Investment Incentive: The Case of Migrant Cocoa Farmers and Settlers in Ivory Coast†. *Journal of African Economies*, 28(2), 147–175. <https://doi.org/10.1093/jae/ejy019>
- Burns, T., C. Grant, K. Nettle, A. M. Britts, and K. Dalrymple. 2006. Land Administration Reform: Indicators of Success, Future Challenges. 13 November. <https://www.landequity.com.au/wp-content/uploads/2019/12/Land-Admin-Reform-Final-Draft-May2007.pdf>
- Burns, A. (2004). *Thailand's 20 Year Program to Title Rural Land*. World Bank. <https://openknowledge.worldbank.org/handle/10986/9213>
- Byamugisha, F. 2016. *Securing Land Tenure and Easing Access to Land*. <https://www.jica.go.jp/jica-ri/publication/booksandreports/175nbg0000004aet-att/175nbg0000004aif.pdf>
- Byamugisha, F. F. K. 2013. *Securing Africa's Land for Shared Prosperity: A Program to Scale Up Reforms and Investments*. Africa Development Forum Series. Washington D.C.: World Bank.
- Cai, Y., H. Selod, and J. Steinbuks. 2018. "Urbanization and Land Property Rights." *Regional Science and Urban Economics* 70: 246–257. <https://doi.org/10.1016/j.regsciurbeco.2018.04.007>
- Cheng, W., N. Zhou, and L. Zhang. 2021. "How does land titling affect credit demand, supply, access, and rationing: Evidence from China." *Canadian Journal of Agricultural Economics/Revue Canadienne d'agroeconomie* 69 (3): 383–414. <https://doi.org/10.1111/cjag.12273>
- Chimhowu, A. (2019). The 'new' African customary land tenure. Characteristic, features and policy implications of a new paradigm. *Land Use Policy*, 81, 897–903. <https://doi.org/10.1016/j.landusepol.2018.04.014>
- Collier, P., E. Glaeser, T. Venables, and P. Manwaring. 2019. *Secure, Legally Enforceable and Marketable Land Rights for Urban Development*. <https://www.theicg.org/wp-content/uploads/2017/08/land-rights-policy-framing-paper-FINAL.pdf>
- Coulibaly, D. A. 2021. *An Analysis of the Impact of Land Tenure Security on Agricultural Productivity in Burkina Faso* (Research Paper 466). African Economic Research Consortium, Nairobi, September.
- Coulibaly, B., G. Sagoe, and L. Shixiang. 2021. "Towards Poverty Alleviation in Developing Countries: An Empirical Study of the Impact of Land Tenure Reforms in Kati, Mali." *PLOS ONE* 16 (3): e0246502. <https://doi.org/10.1371/journal.pone.0246502>
- Cuantarias, Fernando and Miguel Delgado. 2004. Peru's Urban Land Titling Program. In *Scaling Up Poverty Reduction: A Global Learning Process and Conference*, Shanghai, May 25-27, 2004. World Bank.
- Deininger, K., F. Xia, T. Kilic, T., and H. Moylan. 2021. "Investment Impacts of Gendered Land Rights in Customary Tenure Systems: Substantive and Methodological Insights from Malawi." *World Development* 147: 105654. <https://doi.org/10.1016/j.worlddev.2021.105654>
- Deininger, K., Ali, D. A., & Alemu, T. (2011). Impacts of Land Certification on Tenure Security, Investment, and Land Market Participation: Evidence from Ethiopia. *Land Economics*, 87(2), 312–334. <https://www.jstor.org/stable/41307216>
- Deininger, Klaus, Clarissa Augustinus, Enemark, Stig; Munro-Faure, Paul. 2010. *Innovations in Land Rights Recognition, Administration, and Governance*. World Bank Study. World Bank. © World Bank. <https://openknowledge.worldbank.org/handle/10986/2519> License: CC BY 3.0 IGO. <https://openknowledge.worldbank.org/handle/10986/2519>
- Deininger, K. and G. Feder. 2009. "Land Registration, Governance and Development: Evidence and Implications for Policy." *World Bank Research Observer* 24 (2): 233–266.
- Deininger, K., Savastano, S., & Xia, F. (2017). Smallholders' land access in Sub-Saharan Africa: A new landscape? *Food Policy*, 67, 78–92.
- Deutsch, R. (2006). 'Beneficiary Assessment of Land Title Recipients under the Land Management and Administration Project (LMAP)'. Phnom Penh: Ministry of Land Management Urban Planning and Construction.
- Do, Q. T. and L. Iyer. 2007. "Land Titling and Rural Transition in Vietnam." *Economic Development and Cultural Change* (Feb): <https://doi.org/10.1086/533549>
- Durand-Lasserve, A., E. Fernandes, G. Payne, and C. Rakodi. 2007. *Social and Economic Impacts of Land Titling Programmes in Urban and Peri-Urban Areas: A Review of the Literature*. Government of Norway, Ministry of Foreign Affairs. <https://www.birmingham.ac.uk/Documents/college-social-sciences/government-society/idd/research/social-economic-impacts/social-economic-impacts-literature-review.pdf>
- Enemark, S., K. C. Bell, C. Lemmen, C., & R. McLaren. 2014. *Fit-for-Purpose Land Administration: Joint FIG/World Bank Publication*. Washington D.C.: International Federation of Surveyors. <https://www.fig.net/resources/publications/figpub/pub60/Figpub60.pdf>
- Feder, G., T. Onchan, and C. Hongladarom. 1987. *Land Ownership Security, Farm Productivity, and Land Prices in Thailand*. World Bank Discussion Paper ARU 66. Washington, D.C. <https://documents1.worldbank.org/curated/pt/493061468914350453/pdf/Land-ownership-security-farm-productivity-and-land-policies-in-Thailand.pdf>
- Field, E. 2007. "Entitled to Work: Urban Property Rights and Labor Supply

- in Peru.” *HE Quarterly Journal of Economics*, November 2007. https://rpd.princeton.edu/sites/rpd/files/media/field_entitled_to_work_qje.pdf
- Galiani, S. and E. Scharrodsky. 2010. *Property Rights for the Poor: Effects of Land Titling* (No. 103). Universidad Nacional de La Plata, Centro de Estudios Distributivos, Laborales y Sociales (CEDLAS). <https://www.econstor.eu/bitstream/10419/127622/1/cedlas-wp-103.pdf>
- Ghebru, H. and S. Holden. 2013. *Links Between Tenure Security and Food Security: Evidence from Ethiopia*. (ESSP II Working Paper 59). International Food Policy Research Institute (IFPRI) and Ethiopian Development Research Institute (EDRI). <https://www.ifpri.org/publication/links-between-tenure-security-and-food-security-evidence-ethiopia>
- Goldstein, M., K. Hounbedji, F. Kondylis, M. O’Sullivan, and H. Selod. 2018. “Formalization Without Certification? Experimental Evidence on Property Rights and Investment.” *Journal of Development Economics* 132: 57–74. <https://doi.org/10.1016/j.jdeveco.2017.12.008>
- Goldstein, M., K. Hounbedji, F. Kondylis, M. O’Sullivan, and H. Selod, H. 2015. *Formalizing Rural Land Rights in West Africa: Early Evidence from a Randomized Impact Evaluation in Benin*. Washington, D.C.: The World Bank. <https://doi.org/10.1596/1813-9450-7435>
- Goldstein, M., & C. Udry. 2008. The Profits of Power: Land Rights and Agricultural Investment in Ghana. *Journal of Political Economy* 116 (6): 981–1022. <https://doi.org/10.1086/595561>
- Hayes, J., M. Roth, and L. Zepeda. 1997. “Tenure Security, Investment and Productivity in Gambian Agriculture: A Generalized Probit Analysis.” *American Journal of Agricultural Economics* 79 (2): 369–382. <https://doi.org/10.2307/1244136>
- Henderson, J. Vernon, Vivian Liu, Cong Peng and Adam Storeygard. 2020. Demographic and health outcomes by Degree of Urbanisation: Perspectives from a new classification of urban areas. European Commission
- Higgins, D., T. Balint, H. Liversage, and P. Winters, P. 2018. “Investigating the Impacts of Increased Rural Land Tenure Security: A Systematic Review of the Evidence.” *Journal of Rural Studies* 61: 34–62. <https://doi.org/10.1016/j.jrurstud.2018.05.001>
- Holden, S. T., K. Deininger, and H. Ghebru. 2009. “Impacts of Low-Cost Land Certification on Investment and Productivity.” *American Journal of Agricultural Economics* 91 (2), 359–373. <https://doi.org/10.1111/j.1467-8276.2008.01241.x>
- Hong, W., Luo, B., & Hu, X. (2020). Land titling, land reallocation experience, and investment incentives: Evidence from rural China. *Land Use Policy*, 90, 104271. <https://doi.org/10.1016/j.landusepol.2019.104271>
- Huang, Z., & Du, X. (2018). Farmers’ attitudes toward land titling and its potential effects on rural development in China. *China Agricultural Economic Review*, 10(3), 425–442. <https://doi.org/10.1108/CAER-10-2015-0130>
- Huntington, H. and A. Shenoy. 2021. *Does Insecure Land Tenure Deter Investment: Evidence from a Randomized Control Trial*. https://people.ucsc.edu/~azshenoy/files/landtenure_permalink.pdf
- ILO. (2017). *Universal social protection to achieve the sustainable development goals*. International Labour Office.
- Indufor (2014). *Analysis on the Costs of Securing Communal Land Rights: New Technologies and Approaches Offer Potential for Scaling Up* (ID 55782). https://rightsandresources.org/wp-content/uploads/RRI-Study-on-Costs-Final-Draft-ID-55782_Aug-20-FINAL.pdf
- Jacoby, H. G. and B. Minten. 2007. “Is Land Titling in Sub-Saharan Africa Cost-Effective? Evidence from Madagascar.” *The World Bank Economic Review* 21(3): 461–485. <https://doi.org/10.1093/wber/lhm011>
- Joel, T. K. E. and K. C. Bergaly. 2020. *Land Tenure Security, Credit Access and Agricultural Productivity in Cameroon* (AERC Research Paper 395). African Economic Research Consortium, Nairobi, January.
- Kan, K. (2021). Creating land markets for rural revitalization: Land transfer, property rights and gentrification in China. *Journal of Rural Studies*, 81, 68–77. <https://doi.org/10.1016/j.jrurstud.2020.08.006>
- Korsaga, S. 2018. *Land Tenure Security, Land-Related Investments and Agricultural Performance in Sub-Saharan Africa: Efficiency or Equity? A Microeconomic Analysis Applied to the Case of Burkina Faso*. 32. <https://halshs.archives-ouvertes.fr/halshs-01699118/document>
- Kusiluka, M. M., & Chwambo, D. M. (2018). Assessing land titles application and uptake in regularised informal settlements in Tanzania. *International Journal of Urban Sustainable Development*, 10(3), 279–291. <https://doi.org/10.1080/19463138.2018.1536661>
- Lanjouw, J. O. and P. I. Levy. 2002. “Untitled: A Study of Formal and Informal Property Rights in Urban Ecuador.” *The Economic Journal* 112 (482), 986–1019. <https://doi.org/10.1111/1468-0297.00067>
- Lawry, S., C. Samii, R. Hall, A. Leopold, D. Hornby, and F. Mtero, F. (2017). “The Impact of Land Property Rights Interventions on Investment and Agricultural Productivity in Developing Countries: A Systematic Review.” *Journal of Development Effectiveness* 9 (1): 61–81. <https://doi.org/10.1080/19439342.2016.1160947>
- Lay, J., Anseeuw, W., Eckert, S., Flachsbarth, I., Kubitzka, C., Nolte, K., & Giger, M. (2021). *Taking stock of the global land rush: Few development benefits, many human and environmental risks. Analytical Report III*. Centre for Development and Environment, University of Bern; Centre de coopération internationale en recherche agronomique pour le développement; German Institute of Global and Area

- Studies; University of Pretoria; Bern Open Publishing. <https://doi.org/10.48350/156861>
- Li, M., W. Zhang, and D. Hayes. 2018. "Can China's Rural Land Policy Reforms Solve its Farmland Dilemma?" *Agricultural Policy Review* 2018 (1): 8-9. <https://lib.dr.iastate.edu/agpolicyreview/vol2018/iss1/4>
- Linkow, B. (2019). Inheritance Practices, Investment Incentives and Women's Control Over Land in Rural Kenya. *Journal of African Economies*, 28(3), 304–322. <https://doi.org/10.1093/jae/ejy025>
- Ludermir, R., & Alvarado, M. L. (2017, September 20). *Urban Land Conflicts and Evictions in Latin America and the Caribbean*. <https://landportal.org/node/61522>
- Mayanja, D., Massa, D., & Okello, J. (2015). *Certificates Of Customary Ownership Experiences from the District Livelihood Support Programme in Uganda* (HS/042/15E). UN-HABITAT. <https://glt.net/download/certificates-of-customary-ownership/?wpdmdl=8103&refresh=61a4ee3f9e6b51638198847>
- Millennium Challenge Corporation. 2021a, January. *Evaluation Brief: Titling to Raise Land Value and Cut Conflict in Mongolia*. Millennium Challenge Corporation. Washington, D.C.. <https://www.mcc.gov/resources/doc/evalbrief-020920-mng-shps>
- Millennium Challenge Corporation. 2021b, March. *Issue Brief: Land 2.0*. Millennium Challenge Corporation. Washington, D.C. <https://www.mcc.gov/resources/doc/issue-brief-land>
- Millennium Challenge Corporation. 2019. *Land Sector Cost-Benefit Analysis Guidance*, May. <https://www.mcc.gov/resources/doc-pdf/land-sector-cost-benefit-guidance>
- Morales, J., C. Lemmon, R. A. de By, A. E. Ortiz Davila, and M. Molendjik. 2021. "Designing All-Inclusive Land Administration Systems: A Case Study from Colombia." *Land Use Policy* 109 (Oct): 105617. <https://doi.org/10.1016/j.landusepol.2021.105617>
- Muchomba, F. M. 2017. "Women's Land Tenure Security and Household Human Capital: Evidence from Ethiopia's Land Certification." *World Development* 98: 310–324. <https://doi.org/10.1016/j.worlddev.2017.04.034>
- Muyeba, S. 2018. "Does Strength of Tenure Rights Among the Urban Poor Improve Household Economies? Contrasting Matero and George in Lusaka City." *International Journal of Urban Sustainable Development* 10 (1), 16–31. <https://doi.org/10.1080/19463138.2017.1383257>
- Nairesiae, E., & Omusula, C. (2019, August 29). *GLII Briefing Note: Status of Land Indicators, SDGs Progress 2019 and Related Efforts*. <https://landportal.org/node/87551>
- National Planning Commission, A Cost-Benefit Note: Implementing the National Land Policy in Malawi - Technical Report, Malawi Priorities, National Planning Commission (Malawi), Copenhagen Consensus Center (USA) and African Institute for Development Policy (Malawi), 2021. https://www.copenhagenconsensus.com/sites/default/files/mp_land_tilting_report.pdf
- Ngango, J. and S. Hong. 2021. *Examining the Relationship Between Farm Size and Technical Efficiency in Rwandan Maize Production*. International Conference of Agricultural Economists, 17–31 August. <https://ideas.repec.org/p/ags/iaae21/314937.html>
- Ngoga, T. H. 2019. *A Quick, Cost-Effective Approach to Land Tenure Regularization: The Case of Rwanda* (p. 20), International Growth Centre. <https://www.theigc.org/wp-content/uploads/2019/03/Land-tenure-regularisation-the-case-of-Rwanda-March19-FINAL.pdf>
- Nishimwe, G., Rugema, D.M., Uwera, C., Graveland, C., Stage, J., Munyawera, S., Ngambirame, G. (2020). Natural Capital Accounting for Land in Rwanda, Sustainability 2020, 12, 5070; doi:10.3390/su12125070
- Piza, C., M. José, and S. Moura. 2011. "How Does Land Title Affect Access to Credit? Empirical Evidence from an Emerging Economy," Working Paper Series 2211, Department of Economics, University of Sussex Business School.
- SDG Land Momentum Group. 2020a. *Five Years Later: Progress towards the SDG Land Rights Commitments*.
- SDG Land Momentum Group. 2020b, September 24. *Progress Towards the SDG Land Rights Commitments*. <https://landportal.org/node/93862>
- Serageldin, M. (2016). *Inclusive Cities and Access to Land, Housing, and Services in Developing Countries*. World Bank, Washington, DC. <https://doi.org/10.1596/24036>
- Singirankabo, U. A., Ertsen, M. W., & van de Giesen, N. (2022). The relations between farmers' land tenure security and agriculture production. An assessment in the perspective of smallholder farmers in Rwanda. *Land Use Policy*, 118, 106122. <https://doi.org/10.1016/j.landusepol.2022.106122>
- Subramanian, A. and P. Kumar. 2019. "Institution and Development: Experimental Evidence of Land Titling on Welfare Gains in India." *SSRN Electronic Journal*. <https://doi.org/10.2139/ssrn.3440171>
- Szimidziera, M. (2021). *Average household size worldwide, by region 2019*. <https://www.statista.com/statistics/1090668/average-household-size-worldwide-by-region/>
- UN-Habitat. (n.d.). *Annual Report 2021 | UN-Habitat*. Retrieved December 8, 2022, from <https://unhabitat.org/annual-report-2021>
- Wehmann, B., & Lange, A. (2019). *Secure Land Rights for All: A key condition for sustainable development*. GIZ. <https://www.giz.de/en/downloads/>

giz2019-en-secure-%20land-tenure-
rights-successful-approaches.pdf

Whitney, E. M., D. B. Cameron, and
P. C. Winters. 2019. "Heterogeneous
Effects of Urban Land Titling: A
Replication of 'Property Rights for the
Poor.'" *The Journal of Development
Studies* 55 (5): 1030–1033. [https://doi.
org/10.1080/00220388.2018.1506576](https://doi.org/10.1080/00220388.2018.1506576)

World Bank. 2019. *Doing Business
2019*. Washington, DC: World Bank.
DOI:10.1596/978-1-4648-1440-
2. License: Creative Commons
Attribution CC BY 3.0 IGO

World Bank. 2017. *Mozambique Land
Administration Project (Terra Segura)
(P164551): Project Information
Document/Integrated Safeguards Data
Sheet (PID/ISDS)*, 19 December. [https://
ewdata.rightsindevelopment.org/files/
documents/51/WB-P164551.pdf](https://ewdata.rightsindevelopment.org/files/documents/51/WB-P164551.pdf)

Wren-Lewis, L., Becerra-Valbuena, L.,
& Hounghedji, K. 2020. "Formalizing
Land Rights Can Reduce Forest Loss:
Experimental Evidence from Benin."
Science Advances, 6 (26): eabb6914.
<https://doi.org/10.1126/sciadv.abb6914>

Zamboni, Y., & Litschig, S. (2016). Audit
Risk and Rent Extraction: Evidence
from a Randomized Evaluation in
Brazil. In Working Papers (No. 554;
Working Papers). Barcelona Graduate
School of Economics. [https://ideas.
repec.org/p/bge/wpaper/554.html](https://ideas.repec.org/p/bge/wpaper/554.html)

*The paper is originally published by
Cambridge University Press on behalf of the
Society for Benefit-Cost Analysis. This is an
Open Access article, distributed under the
terms of the Creative Commons Attribution
licence ([http://creativecommons.org/licenses/
by/4.0](http://creativecommons.org/licenses/by/4.0)), which permits unrestricted re-use,
distribution and reproduction, provided
the original article is properly cited.*

© The Author(s), 2023.

*The paper is published with
authors' permission. To be
concluded in October issue.* 

Not everyone is prepared for Premium; sometimes, 'good is good enough.'



**says Alexander Wiechert, CEO at
Vexcel Imaging in an interview with
Coordinates at the launch of new
Ultracam Aerial systems**

Continuing the expansion of Ultracam universe, congratulations on the newly launched Ultracam aerial systems - Merlin 4.1 and Dragon 4.1. Please highlight few important features of both.

Thank you so much, we are excited about the new systems as well. For us, this marks an important step into camera segments where we were previously absent. Vexcel has always been a leading provider of digital aerial cameras in the so-called Premium segment, built on the sophisticated pan-sharpening methodology for the utmost image quality. Examples of our Premium line cameras include the UltraCam Eagle, UltraCam Osprey, UltraCam Condor, and the DMC-III.

However, we understand that not everyone is prepared for Premium; sometimes, 'good is good enough.' Therefore, we have decided to launch a camera family in the Fundamental camera segment - the UltraCam Merlin 4.1, which uses high-end Bayer pattern sensors. Bayer pattern-based cameras have a simpler system concept and are typically more affordable, but this comes at the cost of slightly lower image quality, such as interpolation artifacts, resolution impact, and noise level. A lot of aerial camera systems are available in the Fundamental segment, including Phase One and DMC-4. Vexcel is setting the standard in this segment by incorporating premium technology, such as premium lens systems, custom-made electronics, Adaptive Motion Compensation, True Pixel Processing, and the UltraMap workflow, to make the UltraCam Merlin 4.1 the leading camera system with true nadir-oriented camera cones. A unique feature of the Merlin is its capability to be upgraded to the Premium UltraCam lineup in case the final missing piece of image quality is required.

The Dragon represents another significant and important step, setting the standard in the so-called Integrated system segment. This segment comprises hybrid sensors, such as the CityMapper, and we are proud to partner with another Austrian technology leader, RIEGL Laser Measurement Systems. RIEGL has developed a fantastic OEM LiDAR module that is a perfect fit for our oblique camera system. Historically, integrated hybrid systems suffered from a balanced performance,

where the LiDAR would restrict mission parameters, and the ratio between camera GSD and LiDAR point density did not match. Flying two independent sensors in a two-hole plane was often more efficient and effective. However, with the new RIEGL LiDAR, the two subsystems of UltraCam Dragon 4.1 align perfectly in parameters such as flight speed, flight altitude, field of view, GSD versus point density, and more.

The new systems, as well as our well-established Premium cameras, are part of Vexcel's commercial offerings and can be purchased without any usage or data rights restrictions.

What is the significance of high-end Bayer pattern sensors that is contained within UltraCam Merlin 4.1?

Bayer pattern sensors are a well-known technology that has existed in digital cameras for decades. They provide a simple and straightforward method for capturing color images with a single sensor. This principle is widely used in standard digital consumer cameras and cell phone cameras. In the digital aerial photography world, these sensors have also been familiar for many years, mainly because they simplify the technical design of the camera, reducing costs. However, due to the inherent limitations of the Bayer pattern, the image quality cannot keep up with the sophisticated pan-sharpening approach. Like any technology, Bayer pattern sensors have their advantages and disadvantages.

Nonetheless, through the combination of Bayer pattern sensors with our Premium lenses and software, we have achieved outstanding results in the Fundamental camera segment. This includes fully nadir-oriented cones with no tilt, eliminating the need for interpolation in the full-frame image. Our approach allows us to deliver leading performance in this segment.

What are the innovations that have gone into Ultracam Dragon 4.1? How unique are its features that ultimately will benefit the end users?

The Dragon incorporates our Premium camera cones for RGB oblique and RGB + NIR nadir image capture and features high-end LiDAR integration. This LiDAR

system employs a regular scan pattern with no oversampling at the edges and no undersampling at the center of the strip, addressing common issues with other LiDAR scanners.

Moreover, the LiDAR system collects five scan lines: one in the true nadir position, as well as two lines at 10 degrees and two at 20 degrees, both backward and forward. This unique and new approach ensures proper point density even in narrow urban canyons and on facades, making the UltraCam Dragon 4.1 the industry-leading system in the Integrated system segment.

Please highlight few points on how cost effective are these aerial systems.

The Merlin stands out as an exceptionally cost-efficient system, boasting an impressive cost-to-strip-width ratio. This efficiency allows for highly cost-effective aerial operations. Additionally, processing is fully supported by the intuitive UltraMap workflow, known for its high level of automation. It is designed to handle a vast number of images in record time, ensuring a swift turnaround once the aerial mission is completed.

Similar cost-effectiveness can be observed with the UltraCam Dragon 4.1, both in terms of its processing workflow and flying efficiency. The great match of camera and LiDAR parameters contributes to the overall cost-efficiency of the system.

The UltraCam Merlin 4.1 is tailored to emerging markets with fundamental imaging needs where budget considerations take precedence over achieving the highest image quality. On the other hand, the UltraCam Dragon 4.1 is well-suited for city mapping, particularly in areas where vegetation within the city is a significant factor, such as many Asian cities.

It's worth noting that the flexibility of these systems allows for camera cones and LiDAR to be activated or deactivated as required for specific projects. Consequently, the UltraCam Dragon 4.1 can be used effectively in various projects that demand high-resolution imagery and high-density LiDAR point clouds, including corridor mapping, coastal surveys, and more. ▽

India launches nationwide CORS

Union Minister of State (Independent Charge) Science & Technology, Dr Jitendra Singh launched state-of-art latest National Survey Network. The nationwide “Continuously Operating Reference Stations” (CORS) Network. It will be operated by the Survey of India, which has set up more than 1,000 CORS stations across India.

In addition to the Geospatial sector, CORS based precision services will also boost auto navigation and machine control-based solution in Agriculture, Mining, Construction, Transport and Civil Aviation sector. This will open new domains of innovation and research and create a Geospatial based ecosystem in these sectors.

CORS data will also aid in various scientific studies like Upper Atmosphere and Space weather studies, Meteorology and weather forecast, Plate motion and Tectonic studies, Seismology and Hydrology etc. Nationwide CORS based services will be available to business and public, which will not only ensure coherence in geospatial data generated by different stake holders by providing them common reference, but will also increase their productivity. pib.gov.in

International GNSS Day

In recognition of the indispensable role that Global Navigation Satellite Systems (GNSS) play in shaping the modern world, and the fundamental GPS frequency that forms the foundation for all GNSS, the Institute of Navigation (ION) proudly proclaims the establishment of “International GNSS Day” on the 23rd of October annually.

This date, written as “10/23” in U.S. date format, captures the frequency of 10.23 MHz, the original heartbeat of all GPS satellites, signals, and receivers. This frequency was later adopted by all other GNSS service providers, serving as the basis of L-band signals for over 100 navigation satellites today.

As a day of celebration, International GNSS Day serves to highlight the global impact of satellite navigation in diverse sectors, including transportation, agriculture, aviation, surveying, and beyond. It provides a platform to recognize the collaborative efforts of nations, organizations, and individuals in advancing GNSS technology. ION pays special tribute to the developers of GPS, celebrating 50 years since its inception this year.

This initiative acknowledges Dr. Joanna Hinks of AFRL for her visionary proposal, extending the logical tradition of International Pi Day to a day dedicated to the marvels of GNSS. In the spirit of celebration, we encourage professionals, enthusiasts, and the public alike to commemorate this day with educational activities, workshops, and festivities. ion.org

Survey to improve precise positioning through SouthPAN seeks OEMs

The Australian and New Zealand governments, with support from FrontierSI, are conducting a survey with original equipment manufacturers (OEMs) to identify the opportunities and barriers for integrating Southern Positioning Augmentation Network (SouthPAN) signal support in GNSS chips, devices and equipment.

SouthPAN is a Satellite-Based Augmentation System (SBAS) in the Southern Hemisphere and provides improved positioning and navigation services in Australia, New Zealand and maritime regions.

Precise positioning from the network offers improved accuracy down to 10 cm. SouthPAN provides augmented and corrected satellite navigation signals directly from the satellite rather than through a mobile phone, providing accuracy that overcomes gaps in mobile internet and radio communications.

SouthPAN early Open Services has been live since September 2022,

and aviation safety-of-life certified SouthPAN services are set to go live in 2028. Safety-of-life certified services are designed to support end users engaging in life risking operations, such as landing an aircraft at an airport.

OEMs of positioning and/or navigation service equipment are asked to share insights on the support of SouthPAN’s three services into chips, devices and equipment. In particular, the company is looking for OEM’s’ views on barriers and opportunities for support of the L1, dual frequency multi-constellation (DFMC) and precise point positioning (PPP) via SouthPAN services. www.ga.gov.au

Rokubun Galileo OSNMA library delivers navigation message authentication

Rokubun, a Spanish GNSS company released a library solution for decoding and processing Galileo Open Service Navigation Message Authentication (OSNMA) for embedded platforms.

The solution is part of the Horizon Europe BANSHEE project, for which Rokubun served as the coordinating, is EU-funded, and is supported by the European Union Agency for the Space Programme (EUSPA). The goal of the project was to develop a hybrid technology that combines Wi-Fi ranging and satellite navigation (including the Galileo OSNMA) to allow for accurate and seamless indoor-outdoor navigation.

The upcoming Galileo OSNMA will provide authenticated navigation data message against data-level spoofing attacks. By delivering data authentication, the free-to-use Galileo OSNMA assures users that the received Galileo navigation message comes from the system itself and has not been modified by, for example, a spoofing attack.

To address this risk, Rokubun’s library enables the Galileo OSNMA in embedded GNSS solutions. The cross-platform, small-footprint library has undergone extensive testing using official EUSPA

test vectors, and all OSNMA algorithms have been validated in real conditions at the European Commission's Galileo testing facilities located at the Joint Research Centre in Ispra, Italy.

The library is organized to be portable, requiring only a working assembler and C compiler that supports ISO C99. To ensure optimal performance and validate user-specific enhancements, such as the utilization of cryptographic accelerators or other system-on-chip/microcontroller specific resources, Rokubun has implemented a hardware-in-the-loop continuous integration/deployment setup.

This setup continuously tests the library against several reference MCU targets, assessing its performance and guaranteeing its reliability. www.euspa.europa.eu

Mate 60 Pro with satellite calling feature

Huawei's new phone enables satellite-supported two-way text message conversations and can make satellite calls. The feature is powered by the BeiDou Navigation Satellite System, which allows devices to send low-capacity data to its satellites, share their locations and receive messages back from the satellites. <https://asia.nikkei.com>

SAgro150 Auto-Steering System

SingularXYZ has released the new SAgro150 automated steering system for precision agriculture, making it easier for farmers to get started with auto-steering. It realizes $\pm 2.5\text{cm}$ auto-steering accuracy for farming tasks. It uses single-antenna solution instead of dual-antenna solution and users no longer need to assemble and install the antenna crossbar. <https://singularxyz.com>

SSC's GPS certifications branch

The United States Space Force's Space Systems Command (SSC) has a specialized branch responsible for certifying GPS accuracy called the GPS Certification Branch. It is a specialized

team within SSC that is responsible for certifying the hardware, software, and firmware used in GPS-based systems.

The certification process involves the evaluation of design and testing for various components of GPS-based systems. This includes user equipment — the devices used by individuals or organizations to receive GPS signals and determine their precise location.

The GPS Certification Branch works with GPS manufacturers, agencies of the U.S. Department of Defense (DOD), and others to establish and maintain certification standards. Collaboration with industry experts, research institutions, and other certification bodies is also an important aspect of the branch's work to stay informed about technological advancements and ensure the certification process remains up to date with the latest developments.

The certification process also includes space segments — the satellites that transmit the GPS signals, monitoring stations, which track and monitor the performance of the GPS satellites, and the terrestrial modules — that provide end user secured and accurate signals.

Certification of hardware, software, and firmware is critical to ensure that GPS systems meet the standards set by the DOD. This certification ensures that the GPS-based systems used by the military and other DOD agencies are reliable, accurate, and secure. It also ensures that they are interoperable and compatible with other military equipment and communication networks.

The assessment process conducted by the GPS Certification Branch involves thorough testing and analysis of the design, performance, and security of the GPS components. This includes assessing the hardware's ability to receive and process GPS signals accurately, the software's ability to interpret and utilize the GPS data effectively, and the firmware's ability to maintain system integrity and security. www.ssc.spaceforce.mil 

Lytx expands AI-powered geospatial solutions

Lytx® Inc. has announced the rollout of its Weather Hazard Alerts, available to all clients as a project within the Lytx Lab tab in their accounts. Weather Hazard Alerts allow fleet managers the option to get notifications based on geospatial criteria and National Oceanic and Atmospheric Administration (NOAA) weather data to facilitate real-time decision making for safer and more efficient driving.

According to the U.S. Federal Highway Administration, of the roughly 5.8 million vehicle crashes each year, approximately 21% are related to adverse weather, which includes rain, sleet, snow, fog, wind, and blowing debris. The new Weather Hazard Alerts overlays NOAA weather warnings (including snow, thunderstorms, floods, tornados, and more) onto fleet maps, allowing fleet managers to set alerts based on specific geographic, timeframe, and weather criteria and be notified as weather conditions become more severe in that particular region. www.lytx.com

Pioneering BVLOS Drone Delivery Trials in Dubai

Dubai Silicon Oasis (DSO), the specialised economic zone for innovation and knowledge and member of the Dubai Integrated Economic Zones Authority (DIEZ), hosted a three-week long Beyond Visual Line of Sight (BVLOS) drone delivery trials conducted by Jeebly LLC and Skye Air Mobility from India.

The testing conducted in cooperation with the Dubai Future Foundation, the Dubai Civil Aviation Authority and Dubai Silicon Oasis, took place at the Dubai Experimental Zone in DSO. The Zone serves as a real-world test-bed for the development, evaluation and demonstration of robotics and autonomous systems. It was established as part of the Dubai Program to Enable Drone Transportation launched in November 2021. <https://jeebly.com> 

SBG Systems unveils Qinertia 4

SBG Systems will release Qinertia 4 on November 7th. It is a superior post-processing software delivering better precision and reliability compared to RTK systems. It is continually updated to incorporate user feedback and add new features.

Qinertia 4 is packed with an array of innovative functionalities that push the boundaries of navigation capabilities. Its enhanced Geodesy engine boasts an extensive selection of preconfigured Coordinate Reference Systems (CRS) and transformations, making it a versatile solution in applications that use diverse geodetic data. Whether you are in land surveying, hydrography, airborne surveys, construction, or any other field requiring precise positioning, the engine ensures seamless and accurate processing in the right datum and coordinate system.

To tackle the challenges of variable ionospheric activity, Qinertia 4 introduces Ionoshield PPK mode. This cutting-edge feature compensates for ionospheric conditions and baseline distances, allowing users to perform Post-Processing Kinematics (PPK) even for long baselines and/or harsh ionospheric conditions. This ensures surveyors achieve centimeter accuracy even in regions with unpredictable ionospheric disturbances.

Another exciting addition to Qinertia 4 is the extended CORS network support. This feature gives users access* to a vast network of 5000 SmartNet Continuously Operating Reference Stations (CORS) for reliable GNSS data processing. These base stations add to the already impressive network of base stations directly available in Qinertia, bringing the total to over 10,000 bases in 164 countries. This global coverage ensures that Qinertia remains a reliable and efficient solution, regardless of geographic location. In addition, users can import their own base station data and verify its position integrity with Precise Point Positioning (PPP). www.sbg-systems.com

Trimble launches new IonoGuard technology

Trimble has introduced Trimble IonoGuard™, a next-generation technology designed to mitigate ionospheric disruptions in positioning and navigation by minimizing performance impacts caused by scintillation or signal noise. It is Available as a downloadable firmware update for Trimble GNSS receivers utilizing the Trimble ProPoint® GNSS positioning engine

Referred to as solar activity, ionospheric disturbances peak every 11 years. The next major disruption, Solar Cycle 25, is expected to peak between 2024 and 2026. Ionospheric activity can directly impact the quality of GNSS signals, leading to the degradation of position accuracy. While this type of disturbance has the greatest impact on high precision GNSS users operating around equatorial and high latitude regions, global disruptions are possible during the height of the solar cycle. www.trimble.com

TerraStar-X precise positioning GNSS correction service in S. Korea

Hexagon's Autonomy & Positioning division and Munhwa Broadcasting Corporation (MBC) have agreed to bring precise positioning to South Korea through the TerraStar-X Enterprise Correction Service. The hardware-agnostic correction service provides instant convergence and lane-level accuracy in automotive, mobile and autonomous applications. hexagon.com

Emlid releases GNSS receiver with tilt compensation

Emlid has launched a GNSS receiver, the Reach RS3. It enables users to survey at large tilt angles while maintaining survey-grade accuracy. The multi-band receiver works both as a base and a rover and comes factory calibrated.

The receiver offers versatile options to get corrections from continuously operating reference stations (CORS), another Reach

device, or a third-party base, so users can mix and match real-time-kinematic (RTK) receivers in a fleet. <https://emlid.com>

Topcon expands construction layout portfolio with LN-50

Topcon Positioning Systems announces the launch of the LN-50 3D laser, the latest addition to the LN layout navigator family of instruments. It has a 50-meter (164-foot) range as compared to the longer-range, full-featured LN-150 that continues to be a mainstay of the Topcon layout portfolio. www.topconpositioning.com

Exail releases INS for mobile mapping

Exail has launched the Atlans 3, its new Inertial Navigation System (INS) dedicated to land and air mobile mapping applications. It is an all-in-one positioning and orientation system integrating unique micro-electro-mechanical systems. Fiber optic gyroscope (MEMS-FOG) hybrid technology and a dual-antenna RTK GNSS receiver are housed within one compact device. The INS offers North-keeping capability at FOG-level performance across a variety of land and air mobile mapping applications. <https://www.exail.com>

EMCORE releases MEMS IMU

EMCORE Corporation has announced the introduction of the TAC-440 MEMS Inertial Measurement Unit (IMU), the world's smallest 1°/hour IMU. It is a higher-performance, form, fit, and function compatible replacement for the Honeywell 1930 and 4930 IMUs.

Performance of the TAC-440 IMU is based on EMCORE's proven quartz MEMS inertial sensor technology. <https://investor.emcore.com>

CHC Navigation introduces rugged LT800H RTK tablet

CHC Navigation (CHCNAV) has announced the LT800H, a rugged, accurate, and versatile RTK GNSS tablet specially designed for geospatial

and mapping operations in the field. Its industrial design ensures robust outdoor performance and data security in any environment. www.chcnav.com

Syntony launches CRPA GNSS receiver

Syntony GNSS has released CERBER, a GNSS receiver embedded in a CRPA solution. A classic CRPA system consists of embedded GNSS antennas and antijamming treatments. However, CERBER relies on the tight integration of a CRPA treatment (with a 4-array antenna) and the embedded GNSS receiver.

The estimation of GNSS direction of arrival (DoA) is enabled and allows the receiver to check whether those DoA estimations are compatible with GNSS constellations or originate from very few directions. Therefore, users will be able to detect and locate spoofing devices or receivers instantly. The receivers are also able to constantly recalibrate the chains of reception based on the DoA and GNSS signals. <https://syntony-gnss.com>

OxTS introduces INS for land and air applications

OxTS has released the xRED3000, its lightest and smallest inertial navigation system (INS) suitable for land- and air-based applications. It uses OxTS lidar inertial odometry (LIO), which takes data from a lidar in post-processing to reduce IMU drift and improve accuracy in areas with poor or no GNSS signal such as urban canyons. The technology also provides a position accuracy of 0.5 m, even after 60 seconds of no GNSS signal. www.oxts.com

Tallysman releases new L-band GNSS antenna

Tallysman Wireless has released the ARM972XF triple-band plus L-Band GNSS antenna. The ARM972XF uses Tallysman's accutenna technology providing GPS/QZSS L1/L2/L5, GLONASS-G1/G2/G3, Galileo E1/E5a/E5b, and BeiDou B1/B2a/B2b + L-Band coverage. The technology

is designed for precision triple-frequency positioning where light weight and a low profile are required.

Tallysman's ARM972XF is a small and lightweight housed triple-band precision mini ARINC GNSS antenna. It has an average phase center variation of less than 10 mm for all frequencies and overall azimuths and elevation angles. Additionally, both models are available with components qualified for low Earth orbit (LEO). www.tallysman.com

Drone to collect geospatial data for coal mine rehabilitation

Carbonix Australia is collaborating with Woolpert to assist with the rehabilitation of one of New South Wales' oldest open cut coal mines, using drone and geospatial data capture technology to help in this transition. The aerial data collected will be instrumental in establishing a balanced mix of grasslands capable of supporting sustainable grazing and native vegetation corridors to enhance habitat connectivity. <https://aamgroup.com>

Phase One introduces PAS Pana

Phase One introduces PAS Pana, which is a seven-camera wide-field system that redefines the landscape of aerial mapping precision and effectiveness. With a strategic configuration comprising five RGB cameras equipped with 150 mm lenses, and two NIR cameras with 70 mm lenses, PAS Pana reaches a total swath of ~ 48,800 pixels across flight direction. Its range of high-resolution images stretch from 2.5 cm Ground Sampling Distance (GSD) to 30 cm GSD. www.phaseone.com

Trimble and Kyivstar partnership

Trimble and Kyivstar, Ukraine are partnering to install a new Continuously Operating Reference Station (CORS) network to provide GNSS correction services across the country. The new network will be built using Trimble's hardware and software positioning technology. www.trimble.com

MARK YOUR CALENDAR

November 2023

GEOINT Innovation Summit

1-2 November 2023
National Harbor, Maryland, USA
<https://geoint.dsigroup.org>

43rd INCA International Congress

06-08 November 2023,
Jodhpur, Rajasthan.
<https://43inca.org>

Trimble Dimensions 2023

6-8 November
Las Vegas, USA
www.trimble.com

GoGeomatics Expo

6-8 November 2023
Calgary, Canada
<https://gogeomaticsexpo.com>

The Smart GEO Expo 2023

8-10 November
Gyeonggi Province
Republic of Korea.
www.smartgeoexpo.kr/fairDash.do

18th International Conference on Location Based Services (LBS 2023)

20-22 November
Ghent, Belgium
<https://lbs2023.lbsconference.org>

The Pacific GIS and Remote Sensing Conference

27 November - 1 December
Suva, Fiji
<https://pgrsc.org>

March 2024

Geo Connect Asia

06 - 07 March 2024
Singapore
<https://www.geoconnectasia.com>

Munich Satellite Navigation Summit 2024

20 - 22 March
Munich, Germany
www.munich-satellite-navigation-summit.org

April 2024

GISTAM 2024

02 - 04 May
Angers, France
<https://gistam.scitevents.org>

IGRSM Conference 2024

29 - 30 April
Kuala Lumpur, Malaysia
<https://conference.igrsm.org>

June 2024

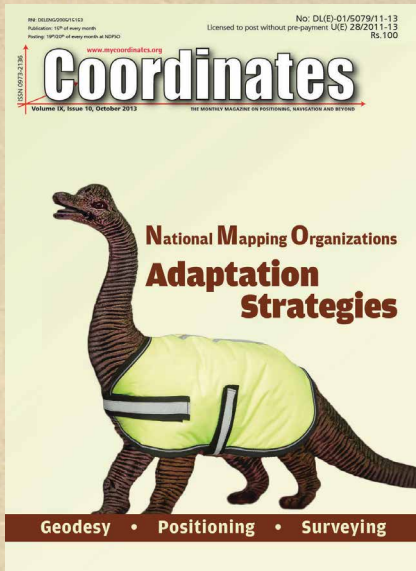
GEO Business 2024

05-06 June
London, UK
<https://www.geobusinessshow.com>

In Coordinates

10 years before...

NMOs: Adaptation strategies



mycoordinates.org/vol-9-issue-10-October-2013

Documenting monuments

Donatella Dominici, Elisa Rosciano, Vincenzo Massimi, Maria Alicandro and Michail Elaipoulos

Department of Civil, Environmental Engineering and Architecture, University of L'Aquila, Italy

In this paper, the laser scanning technique correctly integrated to precise geodetic networks has been tested in two monumental buildings. Both the obtained 3D models featured global metric precision up to 5mm.

I strongly feel that there will always be a requirement for authoritative data, even though ever increasingly it will be exposed to the customer in many different ways, and believe that national mapping authorities can work alongside private organisation and open source providers to meet the changing needs of the customer.

- **Dr Vanessa Lawrence CB**, Ordnance Survey Director General and Chief Executive, UK

JUPEM's aim is to connect the geospatial community with the non-geospatial community in order to be Spatially Enabled Government and Society in the year 2020.

- **Datuk Prof Sr Dr Abdul Kadir Bin Taib**, Director General of Survey and Mapping Malaysia

We now allow them to get direct access to our web map data for their applications, free of charge. This provision has led many vendors to develop new applications that employ our web map data on the web, PCs, tablets and smart phones, and has enhanced the user accessibility to our data.

- **Hiroshi Murakami**, Director General, Planning Department, Geospatial Information Authority, Japan

The focus for today's surveyor should be able to deliver geospatial products at a much faster rate.

- **Prof Peter Chigozie Nwilo**, The Surveyor General of the Federation, Nigeria

I always ponder a lot to satisfy the growing needs and aspirations of our citizens. I emphasized more on providing service, than that of mapmaking. Digital environment gives the extra boost in respect of time and volume of works which could not be easily done by analogue methods.

- **Brigadier General Md Wahidul Islam Talukder NDC, AFWC, PSC** Surveyor General of Bangladesh

It is necessary to use all scientific and technical developments for the benefit of our citizens and to find optimal solutions for their problems and daily suffering so that those plans and strategies are reflected positively on their living standard and daily life.

- **Brigadier General DrEng Awni Khasawneh**, Director General of Royal Jordanian Geographic Centre Director General of Regional Center for Space Science and Technology

By making great strides toward being a citizen-centric organization, the agency envisions a geospatially empowered Philippines by 2020, a vision wherein the government capitalizes on geospatial information for effective governance and a citizenry that benefits from the use of such information.

- **Dr Peter N Tiangco**, The National Mapping and Resource Information Authority (NAMRIA) Administrator, Philippines

NMOs across the world are facing challenges due to penetration of GIS technology and advancements in mobile and GPS technologies. So I in India is gearing itself up and preparing to face these challenges with its programmes.

- **Dr Swarna Subba Rao**, Surveyor General of India

Even with the ongoing technology evolution, the requirement for authoritative data is crucial, which reinforces the role to be played by national government institutions in providing the proper geospatial framework.

- **Luiz Paulo Souto Fortes**, PhD, Brazilian Institute of Geography and Statistics (IBGE), University of the State of Rio de Janeiro (UERJ)



0.05°
ATTITUDE

0.02°
HEADING

1 cm
POSITION

NEW ELLIPSE-D

The Smallest Dual Frequency & Dual Antenna INS/GNSS

- » RTK Centimetric Position
- » Quad Constellations
- » Post-processing Software



Ellipse-D
RTK Dual Antenna



Ellipse-N
RTK Single Antenna



OEM
RTK Best-in-class SWaP-C